Title

The electrical response of carbon nanotube-based thin film sensors subjected to mechanical and environmental effects

Journal

Smart Materials and Structures, 22(2)

ISSN

0964-1726

Authors

Loyola, Bryan R
Zhao, Yingjun
Loh, Kenneth J
et al.

Publication Date

2013-02-01

DOI

10.1088/0964-1726/22/2/025010

Peer reviewed

The electrical response of carbon nanotube-based thin film sensors subjected to mechanical and environmental effects

Bryan R Loyola[1], Yingjun Zhao[2], Kenneth J Loh[2,*], Valeria La Saponara[1,#]
[1]Department of Mechanical and Aerospace Engineering, University of California, Davis, Davis, CA 95616
[2]Department of Civil and Environmental Engineering, University of California, Davis, Davis, CA 95616

[*]Co-corresponding E-mail: kjloh@ucdavis.edu
[#]Co-corresponding E-mail: vlasaponara@ucdavis.edu

Abstract. Fiber-reinforced polymer composites are a popular alternative to traditional metal alloys. However, their internally occurring damage modes call for strategies to monitor these structures. Multi-walled carbon nanotube-based polyelectrolyte thin films were manufactured using a layer-by-layer deposition methodology. The thin films were applied directly to the surface of glass fiber-reinforced polymer composites, with the purpose of structural monitoring. This work focuses on characterizing the sensitivity of the electrical properties of the film using time- and frequency domain methods under applied quasi-static and dynamic mechanical loading. In addition, environmental effects such as temperature and humidity are varied to characterize the sensitivity of the electrical properties due to these phenomena.

1. Introduction

Fiber-reinforced polymer (FRP) composites are utilized as a variety of structural components for their high strength-to-weight ratios, resistance to corrosion and fatigue, and conformability. Examples include aerospace, civil, automobile, wind turbine, and naval structures. They are a popular alternative to traditional monolithic alloys. For instance, the Boeing 787 Dreamliner that was released in October 2011 has a structure that is more than 50% composite material by weight, with the majority consisting of carbon FRP composites [1]. In contrast, wind turbine blades typically consist of glass FRP composites due to their low cost and high specific strength, as compared to structural metals [2].

Despite many desirable traits, composite materials can and do sustain damage when subjected to various loading scenarios, including impact, excessive loading, fatigue, material defects, environmental deterioration, improper manufacturing, and fluid penetration. Damage induces failure modes such as delamination, fiber and matrix breakage, fiber-matrix debonding, matrix swelling, and matrix and fiber deterioration. In general, these damage modes tend to manifest internally to the composite structure, and this minimizes the ability to use visual inspection for damage detection. This is a problem, since visual inspection is the predominant method of non-destructive evaluation in many disciplines, including aerospace and civil structures. Undetected structural damage can propagate, eventually leading to catastrophic structural failure [3].

As a result of the shortcomings of visual inspection, several alternative damage detection approaches have been developed and applied to this very urgent problem. Examples of structural health monitoring (SHM) techniques that have been developed for or applied to composite damage detection include optical fibers [4], acoustic emission [5], ultrasonic sensors [6], strain gauges [7], and shape memory alloys [8], to name a few. All of these methods have shown promise in their capability to capture various modes of damage, but they also have drawbacks that need to be addressed by complementary methodologies. Many of these systems require expensive and bulky hardware and data acquisition systems, such as optical fibers and ultrasonics- and acoustic-based methods. When embedded in composite materials, these sensors have been shown to diminish composite mechanical properties (*e.g.*, optical fibers over 100 μm in diameter [9] or piezoelectric disks for ultrasonic monitoring [10]). It is for these reasons that many groups have pursued other sensing approaches that directly modify the composite material. An example is to develop strain sensitive FRP composites by embedding nanomaterials within their epoxy matrix. Monitoring the integrity of the structure can be achieved by probing its electrical properties, and the method does not adversely affect the mechanical properties of the structure.

The discovery of carbon nanotubes [11] and the identification of their unique material properties [12] has brought forth widespread attention to the use of this material for various sensing applications. Carbon nanotubes are typically introduced into FRP composites in two distinct ways: as an additive to the polymer matrix or as a thin film within or upon the composite. These applications take advantage of the high mechanical and electrical properties intrinsic to single-walled (SWNT) and multi-walled carbon nanotubes (MWNT) [13]. Some examples of this work are CNT-epoxy nanocomposites [14], neat CNT mats (*i.e.*, buckypapers) [15, 16], and other polymer nanocomposites thin films [17, 18]. It has been found that CNT-based nanocomposites are piezoresistive, where their electromechanical response changes with applied strain and can be linear [16], non-linear [19], and/or multifunctional [20]. In addition to strain sensitivity, these films are also sensitive to environmental changes such as temperature [21] and humidity [22]. This type of environmental sensitivity in a sensor is common, with some examples including metal-foil strain gages [23] and fiber-Bragg gratings [24]. Thus, prior to using CNT nanocomposites for SHM, a full characterization of their sensing and environmental response is needed.

The purpose of this study is to characterize the strain sensing and environmental sensitivity response of MWNT-based thin films manufactured using a layer-by-layer fabrication process. Films of different thicknesses have been deposited directly onto the surface of glass fiber-reinforced polymer (GFRP) composites for direct strain sensing. The responses from these tests are complementary to the work previously performed on thin films embedded in GFRPs for *in situ* strain sensing [20]. First, strain sensing characterization of film-enhanced GFRP substrates have been performed by loading them in monotonic uniaxial tension, low-cycle dynamic, and high-cycle dynamic load patterns. Thin film electrical properties have been measured simultaneously using time- and frequency-domain methods. Secondly, their environmental responses have been determined by measuring the electrical response of the films at a wide range of temperature and humidity levels. These responses have been fully characterized by curve fits motivated by physics-based models.

2. Experimental Methods

To demonstrate the capability of these films as an alternative for SHM of FRP composites, the MWNT-based thin films were deposited onto GFRP substrates upon which all of the mechanical, thermal, and humidity tests were performed.

2.1 Film Fabrication

The deposition of the MWNT-based thin films upon the GFRP substrates was performed by a layer-by-layer (LbL) process that allows for nano-scale control of film deposition [25, 26]. The substrates used were quasi-unidirectional glass fiber weaves (type 7715, Applied Vehicle Technology) that were impregnated with a two-part epoxy (125 resin / 237 hardener, Proset Inc.) and cured to specification for

Figure 1. Pictorial representation of a layer-by-layer manufactured (MWNT-PSS/PVA)$_n$ thin film. PSS chains (helical red lines) wrapped around MWNTs (straight black lines) with deposited PVA (thin blue lines).

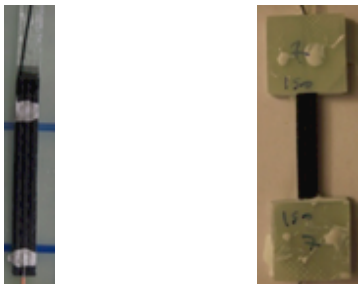

(a) (b)

Figure 2. (MWNT-PSS/PVA)$_n$ thin film deposited onto GFRP substrates before (a) and after (b) tabbing.

15 h at 25 °C and 8 h at 80 °C. The substrates were cut to 25 x 75 mm^2 and were thoroughly cleaned with water and isopropyl alcohol prior to mounting them in the LbL deposition system. Layer-by-layer film assembly is based on the sequential deposition of opposite-charged materials onto a substrate such as the GFRP specimens used in this study [25]. To deposit the first monolayer, the LbL system was programmed to immerse the substrates in a 0.5 wt.% poly(vinyl alcohol) (PVA) solution for 5 min. The substrates were then rinsed for 3 min in deionized water and then dried with compressed air for 5 min. Then, the dried substrates were transferred to a 1.0 wt.% poly(sodium 4-styrenesulfonate) (PSS) solution with 1 mg·mL^{-1} of dispersed MWNTs (Cheap Tubes). The dispersal of the MWNTs into the PSS solution was accomplished by 180 min of bath sonication (135W, 42 kHz), followed by 1 h of tip sonication (3 mm tip, 150 W, 20 kHz). This two-step sonication process ensured a fully stable MWNT-PSS suspension [18, 20]. Finally, the substrates were rinsed again for 3 min and dried for 5 min, so as to remove any loosely adsorbed polyelectrolyte and nanotubes. This process was repeated for a specified number of times, each time depositing a single bilayer of the thin film (figure 1). Numerous thin films were manufactured with 25, 50, 75, 100, and 150 bilayers.

The thin films resulting from this process were extremely robust, due to the chemical bond formed between the substrate to the film constituents and between the thin film chemical species. Popular thin film constituents for the LbL process are polyelectrolytes of opposite ionic charge facilitating electrostatic assembly of the thin film, of which PSS and PVA are both members of this chemical family. However, PSS and PVA bond through strong hydrogen bonding that created a more robust film [27]. The MWNTs were bound within this polyelectrolyte matrix via polymer wrapping by the PSS, which has wound chains around each MWNT to reduce MWNT hydrophobicity [28]. A previous study of freestanding CNT-PSS/PVA films had been reported and validated the impressive mechanical properties resulting from the chemical associations between the film constituents [29].

2.2 Specimen Preparation and Electrical Characterization

With the aim to characterize the electrical response of the thin film to mechanical, thermal, and hygroscopic conditions, uniform specimens and electrical characterization methods were used as a means to remove any dimensional effects on the sensitivities of the thin films. The ASTM standard for characterizing the tensile properties of FRP composites was consulted for determining specimen size [30]. Due to the setup used for film deposition, only 40 mm of the 75 mm length of the substrate was deposited with (MWNT-PSS/PVA)$_n$ films (where the subscript *n* indicates the number of bilayers). Following the ASTM suggestion of a 1:11 width-to-gauge length ratio, the width of the specimens was set to 3 mm for a 25 mm gauge length. In order to protect the electrodes from strain effects, the electrodes were placed

outside of the gauge length with an electrical gauge length of ~28 mm. Two-point probe electrical measurements were used due to the limited space on the specimen. Contact resistance was minimized by using conductive silver paint as electrodes (figure 2a). To protect the substrates from damage from the grips during mechanical testing, G-10 GFRP tabs were applied to opposite ends of each specimen with a high strength adhesive (Hysol 903, Henkel Corp.). An example of a finished electromechanical specimen is presented in figure 2b.

Measurement of $(MWNT\text{-}PSS/PVA)_n$ thin film electrical properties were performed using time-domain direct current (DC) resistance measurements and frequency-domain electrical impedance spectroscopy (EIS). The DC resistance measurements were performed using an Agilent 34401A digital multimeter with 6.5 digit accuracy. The EIS responses were taken using an Agilent 4294A impedance analyzer over a frequency range of 40 Hz to 110 MHz.

2.3 Mechanical Strain Sensitivity Characterization

The strain sensing response of $(MWNT\text{-}PSS/PVA)_n$ thin films were characterized by measuring their time-domain DC electrical resistance and frequency-domain impedance responses during applied mechanical loading. Three different sets of loading patterns were applied to specimens fabricated with different film thicknesses (namely, 25, 50, 75, 100, and 150 bilayers): monotonically increasing strain to failure, low-cycle dynamic strain patterns, and high-cycle dynamic strain patterns. All mechanical tests were performed on a TestResources 150R load frame equipped with a 4.48 kN load cell with serrated grips. The displacement and angular position of the load frame crosshead was verified using two laser displacement sensors (Microtrak II, MTI Instruments).

2.3.1 Monotonic Uniaxial Tension Tests

The full range of the $(MWNT\text{-}PSS/PVA)_n$ films' strain sensitive response was characterized by applying monotonically increasing strain to each film-coated GFRP substrate until failure. The load frame displacement is fixed at 2 $mm \cdot min^{-1}$ based on ASTM 3039 standard. In order to measure the change in electrical properties at fixed strain values, the crosshead displacement was held at specified strain values for a 60 s period, when both the DC resistance and EIS measurement were obtained. These specified strain values were every 1,000 με from 0 to 10,000 με and every 5,000 με thereafter. This measurement pattern allowed for higher resolution at lower applied strains, while limiting the number of pauses to minimize any effects of creep.

2.3.2 Low-cycle Dynamic Tests

Three-cycle tensile dynamic load tests to 8,000 με and to 25,000 με were conducted on film-enhanced GFRP specimens for characterizing thin film electromechanical responses to repeated loading and unloading. During each cycle of loading, a 60 s pause was taken at 25% increments of the total strain. As before, these pauses were for DC resistance and EIS measurements. The two different strain amplitudes were chosen based on results obtained from Section 2.3.1 and allowed for probing the two regions of the bi-functional electrical response.

2.3.3 High Cycle Dynamic Tests

As the long-term intent for these films is implementation as a SHM sensor, it is important to understand how the electrical properties of thin films change after numerous cycles of mechanical loading. To this end, specimens were subjected to 1,000 cycles of sinusoidal-cyclic loading from 0 to 8,000 με at a frequency of 1 Hz. A 60 s pause was taken at a strain value of 4,000 με every 100 cycles to measure the film's DC resistance and EIS response. The strain amplitude was determined using the same logic as in the low-cycle dynamic tests described in Section 2.3.2.

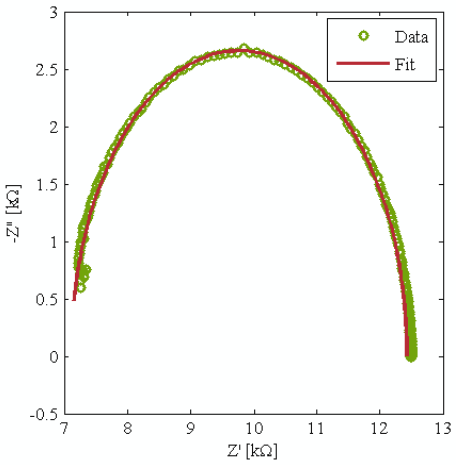

Figure 3. Example of an $(MWNT\text{-}PSS/PVA)_n$ EIT response and the corresponding fit to the equivalent circuit model.

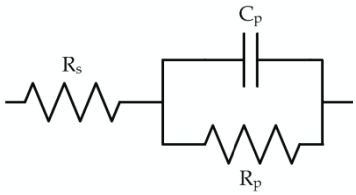

Figure 4. Circuit diagram of the equivalent circuit model representing the EIS response of the films

2.4 Thermal Testing

The effects of temperature change to the films' electrical properties were characterized by subjecting specimens to monotonically increasing temperatures from ambient to 100 °C (in increments of 5 °C) in a convection oven. To test all specimens under the same conditions, five specimens each with thicknesses 50, 75, 100, or 150 bilayers were attached to a pristine sheet of G-10 using high-temperature kapton tape. Only one end of each specimen was affixed to the G-10 GFRP to allow unconstrained thermal expansion to occur. DC resistance measurements were taken at each temperature step after the specimens had come to thermal equilibrium.

2.5 Humidity Testing

Another environmental factor taken into account was the effect of humidity on the electrical properties of the $(MWNT\text{-}PSS/PVA)_n$ films. As with the thermal tests (Section 2.4), five specimens each with thicknesses of 50, 75, 100, or 150 bilayers were mounted onto a G-10 GFRP sheet. The sheet of specimens was placed in an environmental chamber set at 35 °C. The chamber was programmed to increase its humidity from 25 to 80 %RH (in 5 %RH increments) and holding at each level for 1 h. The humidity and temperature of the chamber were verified using a temperature and humidity probe that takes a measurement every 10 s. The 20 specimens were connected to an Agilent 34970A with an armature multiplexer card to simultaneously measure DC resistances of each specimen every 5 s.

3. Results and Discussion

3.1 EIS Equivalent Circuit Fitting

A typical $(MWNT\text{-}PSS/PVA)_n$ thin film EIS response is plotted on a Nyquist plot, as shown in figure 3, and this semi-circular trend is consistent with the response of other CNT thin films [17, 31]. To extract the underlying electrical properties of the film from this response, the spectrum is typically fit to a physics-based equivalent circuit model. The characteristic equivalent circuit model for a response such as the one in figure 3 is a series resistor (R_s) connected to a resistor (R_p) and capacitor (C_p) in parallel (figure 4). This circuit model has been used to describe a similar EIS response of a zirconia-yttria solid electrolyte film, where the series resistor models the mean grain resistance, and the inter-grain effects are

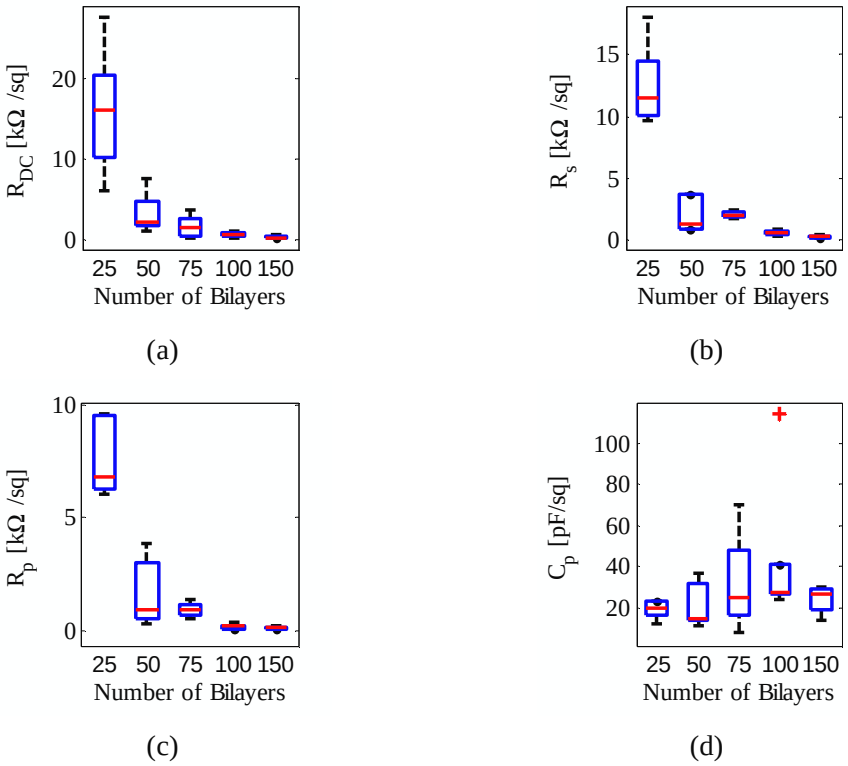

Figure 5. Unstrained electrical properties of $(MWNT\text{-}PSS/PVA)_n$ films as a function of film thickness plotted in a boxplot. The box indicates the interquartile region and the line within it signifies the median of the data. The red crosses represent outlier values.

modeled by the parallel resistor and capacitor [32]. The impedance equation that corresponds to the equivalent circuit shown in figure 4 is represented in equation (1):

$$Z(\omega) = Z'(\omega) + iZ''(\omega) = \left(R_s + \frac{1/R_p}{(1/R_p)^2 + \omega^2 C_p^2} \right) - i\left(\frac{\omega C_p}{(1/R_p)^2 + \omega^2 C_p^2} \right) \quad (1)$$

Fitting of this highly non-linear model to the EIS spectra is achieved using the non-linear least squares solver function in *MatLab*.

3.2 Thin Film Electrical Properties: Unstrained

Before the mechanical, thermal, or humidity sensitivities of the films are discussed, it is important to characterize the baseline electrical properties of the $(MWNT\text{-}PSS/PVA)_n$ thin films as a function of thickness. The initial unstrained time- and frequency-domain electrical measurements from all of the mechanical experiments were compiled into boxplots as shown in figure 5. Figure 5a shows the films' unstrained DC resistance, whereas figures 5b-d present the numerically fitted equivalent circuit parameters based on figure 4. It can be seen from figure 5 that the median and interquartile range of the DC resistance and resistive equivalent circuit elements reduce significantly with increasing number of bilayers. This is consistent with power law-type response of particle-infused polymer composites (*i.e.* nanocomposites), particularly in the post-percolation region [33-36]. As for the capacitance of the films, figure 5d indicates that the capacitance stays relatively constant over the range of thin film thicknesses tested. Similar trends have also been identified by Loh *et al.* [18].

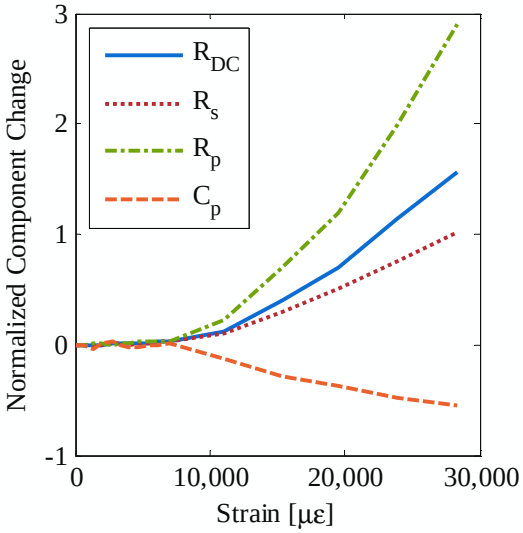

Figure 6. DC resistance and EIS fitted circuit elements response to monotonically increasing strain

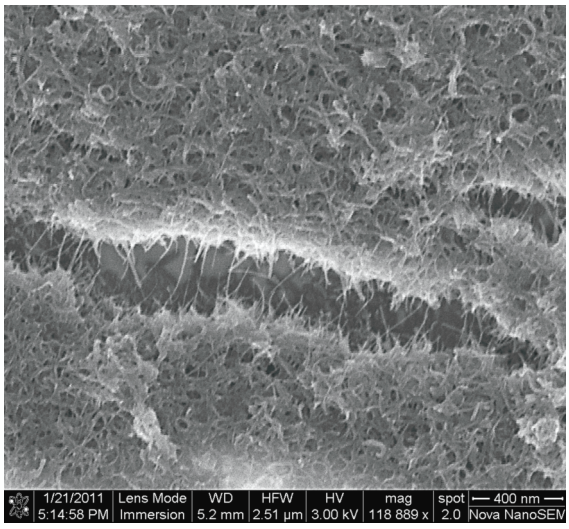

Figure 7. SEM image of damage to the $(MWNT\text{-}PSS/PVA)_n$ film.

3.2 Uniaxial Tensile Electromechanical Response

As mentioned in Section 2.3.1, monotonic uniaxial tests have been conducted on GFRP specimens with $(MWNT\text{-}PSS/PVA)_n$ films for characterizing the full range of thin film strain sensitivity. Both DC resistance and EIS data have been obtained, and EIS responses have been fit to the parallel resistor-capacitor circuit shown in figure 4. In order to directly compare different circuit elements' dependency on strain, all of the DC resistance and EIS equivalent circuit elements are presented as normalized changes relative to the initial unstrained parameter measurement. For example, calculation of normalized resistance uses equation (2), where R_0 is the unstrained resistance value.

$$R_{norm} = \frac{\Delta R}{R_0} \tag{2}$$

An example of a full strain response is presented in the plot shown in figure 6. The responses by all of the electronic parameters are bi-functional in nature. For the resistive parameters, there exists a positive relationship between normalized changes in resistance as a function of increasingly applied tensile strains. Several other groups have also found that CNT-based films increase their resistivity in tandem with increasing tensile strains [16, 31, 37]. In addition, Thostenson and Chou [38] and Shindo *et al.* [39] have also observed this bi-functional response comparable to figure 6, although these studies have not explored the frequency-domain EIS response of CNT-based nanocomposites. The initial functional response is generally considered due to MWNT stretching or rigid-body motion of MWNTs within the compliant polymer matrix, while the second functional response is due to damage in the film in the form of micro-cracking of the composite substrate [14, 39]. This damage can be seen in the scanning electron microscope (SEM) image shown in figure 7. On the other hand, film capacitance change is near zero during the first response region while decreasing after the application of large tensile strains.

Upon identification of the bi-functional circuit parameter responses to applied strain, it has been found that a linear-quadratic model can adequately fit the films' electromechanical responses. The quadratic element of this model is not currently associated with a particular physical effect; however, this will be the focus of future work. The model has been applied as follows. First, the transition point of the bi-functional response (*i.e.,* from low strain to high strain) has been manually identified and recorded. Then,

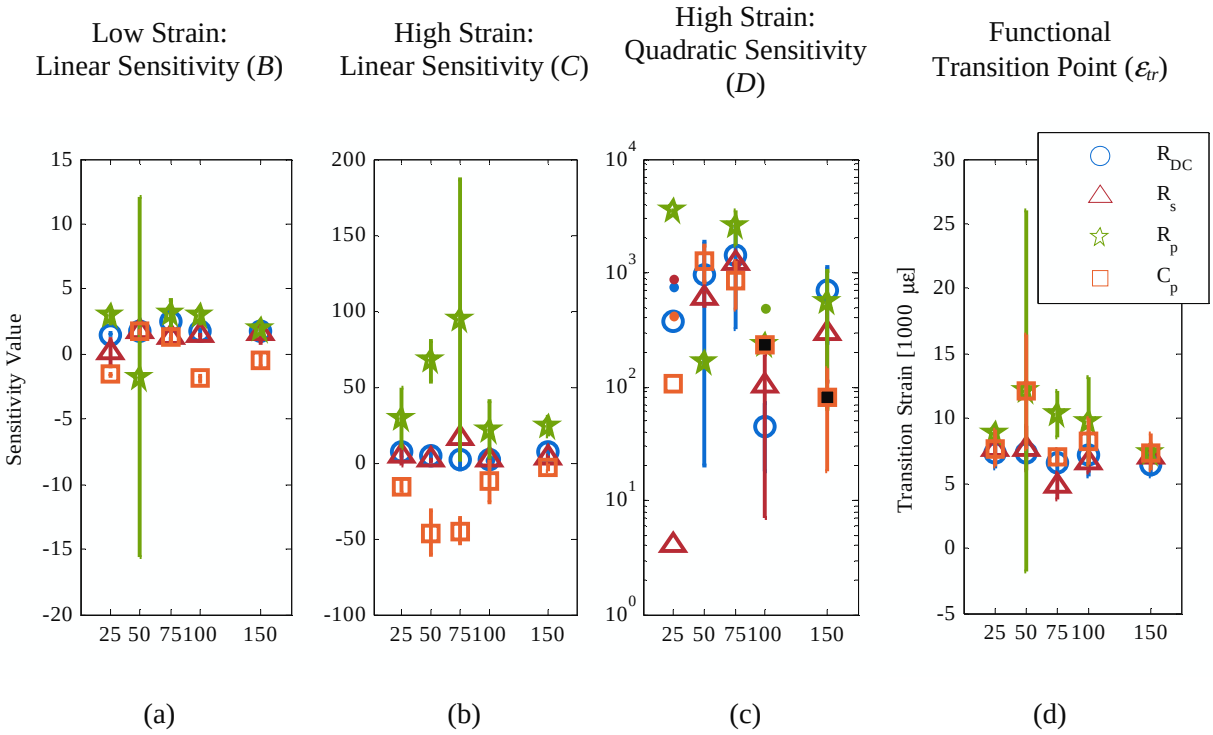

Figure 8. Linear-quadratic sensitivities obtained from fits to equation (2). Black-filled symbols indicate negative values and error bars substituted with dots indicate lower bound is a negative value in (c).

the linear-quadratic model has been fit to each data set using the non-linear least squares fit function 'lsqnonlin' in MATLAB. The equation of the linear-quadratic model is also shown as follows:

$$\frac{\Delta R}{R_0}(\varepsilon)=\frac{1}{2}\left(1-erf\left(\varepsilon-\varepsilon_{tr}\right)\right)\cdot\left(A+B\varepsilon\right)+\frac{1}{2}\left(erf\left(\varepsilon-\varepsilon_{tr}\right)+1\right)\cdot\left(A+B\varepsilon_{tr}+C\left(\varepsilon-\varepsilon_{tr}\right)+D\left(\varepsilon-\varepsilon_{tr}\right)^2\right) \quad (3)$$

The transition between the functional responses was facilitated using the error function, noted as *erf( )* in the equation. The error function is a sigmoidal function that has a smooth but sharp transition from -1 to 1 and can be shifted and scaled to create the same transition between 0 and 1.

With the thin film time- and frequency-domain electrical responses fit to the linear-quadratic model, the medians of the results are presented in figure 8 in terms of the low-strain linear sensitivity (*B*), the high-strain linear sensitivity (*C*), the high-strain quadratic sensitivity (*D*), and the bi-functional transition point (ε_{tr}) in terms of number of bilayers. The error bars that accompany each result are a measure of the median absolute median deviation, which is a robust measure of the variability of the results.

Two distinct trends are apparent by examining the fitted sensitivity parameter sin figure 8. The sensitivities of R_{DC} and R_S are statistically similar in both the low- and high-strain regimes. Within the low strain regime, these sensitivities are linear between 1 and 2.5, for all film thicknesses, and exhibit an increase of the linear sensitivities by less than a multiple of three in the higher strain regime. This is in contrast to the responses of the parallel equivalent circuit elements, although the two responses appear to be correlated with one always being positive and the other negative. In the transition between the functional responses, the sensitivities of the parallel equivalent circuit elements demonstrate an increase in linear sensitivities by one to two orders of magnitude with a drastic increase of sensitivity variability. This has been verified in previous work with CNT-based thin films using acoustic emission responses

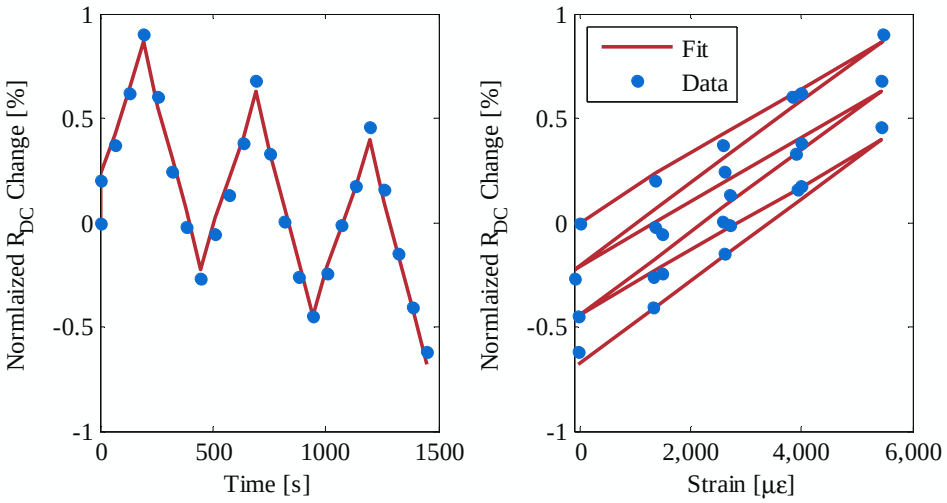

Figure 9. Example R_{DC} response to dynamic loading to a magnitude of 8,000 με with the corresponding fit to (4) with and $R^2 = 0.98$.

[40], and a model incorporating transverse crack propagation [39] shows that this high strain regime is dominated by the response of the film to damage transferred from the damaged substrate. It is felt that this demonstrates a higher sensitivity of the parallel equivalent circuit elements to damage in the thin film as compared to the sensitivities of R_{DC} and R_S. It is not fully understood why a similar correlation is not found in the quadratic sensitivities of the fitted electrical responses in the high strain regime.

Despite the differences in the linear sensitivities between R_{DC} and R_S and that of the parallel equivalent circuit elements in the low- and high-strain regimes, the strain at which this transition occurs is statistically consistent among all films thicknesses and electrical property parameters. This further reinforces that the change in the response of the electrical properties is indeed due to a physical change, where this transition has been found to be due to the onset of damage within the composite substrate, as have been demonstrated by [39, 40].

3.3 Dynamic Strain Response

In addition to monotonic uniaxial tensile tests, films have also been subjected to three-cycle tensile tests to 8,000 με and 25,000 με, as have been described in Section 2.3.2. As discussed earlier, these strain amplitudes have been chosen to understand the represented loading effects in both of the response regimes demonstrated by the films during monotonically loaded tests (Section 3.2).

The responses of the thin films during the lower magnitude dynamic tests to 8,000 με are very consistent among the different specimens tested. An example of this behavior can be seen in figure 9, where the DC resistance linearly drops over time, but the film's piezoresistivity remains constant over time. To model this response, a simple linear-time and linear-strain response equation is fit to each data set, as is described in equation (4):

$$\frac{\Delta R}{R_0} = \alpha t + S\varepsilon \tag{4}$$

All of the low-magnitude dynamic responses are fit to equation (4) using the non-linear fitting function in *MatLab*. The strain sensitivities of the fits for all specimens tested are reported in Table 1. The results for the capacitive elements are left out, because the fits did not reveal any meaningful trends. Among all of

Table 1. Strain sensitivity parameters for 8,000 με dynamic testing.

Bilayers:	25	50	75	100	150
R_{DC}	2.33 ± 0.11	1.70 ± 0.13	2.26 ± 0.26	2.40 ± 0.52	2.10 ± 0.52
R_S	2.22 ± 0.07	1.58 ± 0.07	2.14 ± 0.46	1.94 ± 0.28	-
R_P	3.30 ± 0.63	2.31 ± 0.06	3.01 ± 0.72	3.04 ± 0.66	-

the resistive elements, the sensitivity to strain is consistent, where sensitivity varies between 1.5 and 3.3. This is very consistent with the findings from the monotonically loaded samples in the linear region (as presented in Section 3.2) as well as other studies on $(CNT\text{-}PSS/PVA)_n$ films [18]. As detailed in Section 3.2, this strain response is believed to stem from stretching and slight reorientation of the MWNTs in the film. It can be seen from Table 1 that the average strain sensitivities corresponding to each thickness set are consistent for R_{DC}, R_s, and R_p.

In addition to reasonably consistent sensitivity to strain, the response of the electrical properties to the dynamic loading drifts over time with a relatively low-magnitude linear dependence. Overall, the magnitude of the drift is on the order of 10^{-4} %·s^{-1}, which can easily be discerned in the representative three-cycle dynamic response shown in figure 9. The direction of the drift is predominantly negative, which is thought to be due to alignment of the carbon nanotubes [31]. A small number of thin films with 100 or 150 bilayers have a very small positive linear trend on the order to 10^{-4} %·s^{-1}, which is thought to be due to the films having a lower bi-functional transition strain than the other films and are slowly accumulating damage within the film. This has been witnessed in other CNT-based thin films [38].

The response of the thin films cycled to 25,000 με is considerably different than that of the 8,000 με cases. Although all responses have demonstrated a general saw tooth-shaped response, the underlying response cannot be fit to a unified model. Nevertheless, figure 10 presents the full DC resistance and EIS circuit element responses for a selected dataset. As is the case with the response to 8,000 με dynamic cycling, the capacitive response is inconsistent between specimens, so these effects will be neglected from comment. Although all of the resistive parameters have a saw tooth shaped response consistent with the shape of the loading, the specific response for each cycle is not consistent. In general, the responses of the electrical properties can be delineated based on their response to increasing and decreasing strains. The response to increasing strain is witnessed to be linear, of a concavely increasing or of a convexly increasing manner. However, the resistive responses to decreasing strain are only of concavely or convexly decreasing magnitudes. This myriad of responses is illustrated by four randomly selected curves in figure 11. It can be seen that not one of those responses match. This phenomenon is not surprising as it has been determined in the monotonically loaded case that the quadratic responses occur when damage is

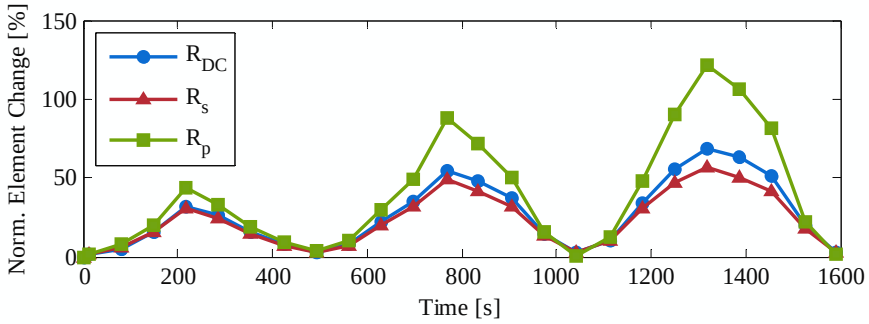

Figure 10. Example resistive parameter response to 25,000 με dynamic strain.

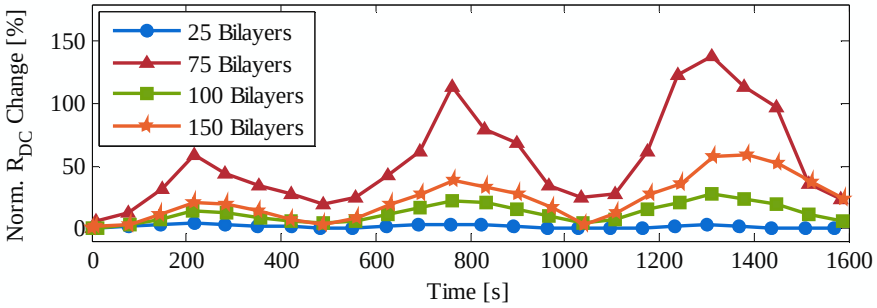

Figure 11. Example DC resistance response to 25,000 με dynamic strain for four thin film thicknesses.

sustained by the film due to cracking and other failure phenomena, thus inducing a more random but general response. As indicated before, this type of response has been observed previously [38, 39].

3.4 High-Cycle Dynamic Strain Sensing Response

To understand how the thin films will perform in real world application with extended deployment, the thin films were subjected to 1,000 cycles of loading as described in Section 2.3.3. As illustrated from a representative electrical response shown in figure 12, the overall change in the resistive measurements with respect to the number of cycles is less than 1% over 1,000 cycles. This is comparable to the time-dependent sensitivity obtained from the three-cycle dynamics tests to 8,000 με and has less drift than previous studies involving repeated dynamic responses with $(SWNT\text{-}PSS/PVA)_n$ films [31]. As with the other dynamic tests, the capacitive results are neglected due to its lack of significance.

3.4 Thermal Effect on Electrical Properties

Due to drastic temperature differentials that various structures can experience during operation, it is important to understand the effects of temperature on sensor electrical properties. Upon conducting the temperature tests as specified in Section 2.4, it has been found that all of the thin films of different thicknesses behaved in the same fashion. An example of the highly non-linear electrical response to the applied monotonically increasing temperature profile is shown in figure 13. This response is characteristic of SWNTs in mats or tangled ropes [41, 42]. This characteristic response has been studied and a mathematical model has been developed to take this behavior into account, which is given in equation (5):

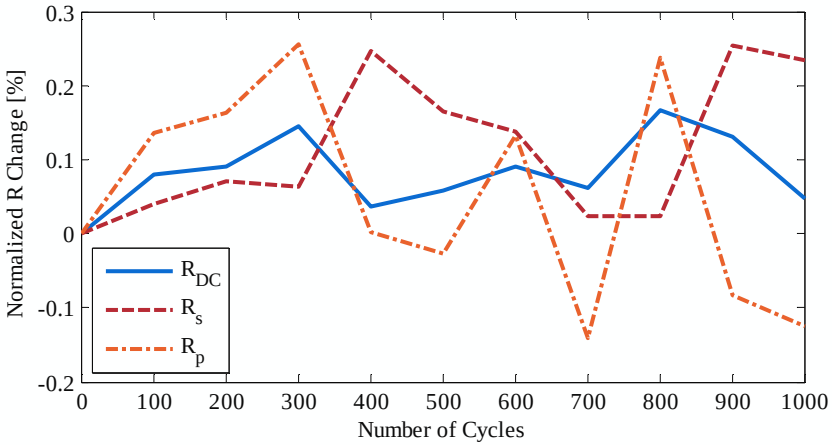

Figure 12. Resistive component response to 1,000 cyclic loadings with a magnitude of 8,000 με of a $(MWNT\text{-}PSS/PVA)_{50}$ film.

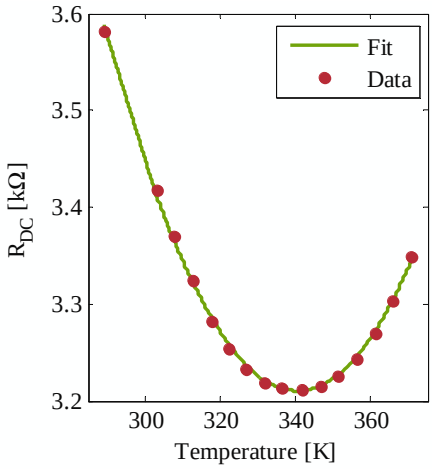

Figure 13. Example DC resistance response to monotonically increasing temperature with corresponding fit to equation (5) with $R^2 = 0.998$.

$$R(T) = R_m e^{-\frac{T_m}{T}} + R_t e^{\frac{T_c}{T+T_s}} \quad (5)$$

The first term of this equations represents the highly-anisotropic conductivity along the MWNTs, where phonons with energies of $k_B T_m$ backscatter charge carriers [41] and is responsible for the $^{dR}/_{dT} > 0$ behavior. This first term is present in the thermal response of SWNTs as well as MWNTs. The second term of equation (5) represents electron transport due to electron tunneling between CNTs. Here T_c and T_s are electron tunneling parameters and represent the combined effect of the nanotube gaps (*i.e.*, due to PSS and PVA). The tunneling components are responsible for the $^{dR}/_{dT} < 0$ behavior in the data. However, this response tends to be the case for SWNTs [43] and not typically for MWNT thin films. In the general MWNT case, the second component tends to be linear in nature and not exponential, as in the case of several studies involving individual MWNTs [44, 45], aligned MWNT buckypapers [46, 47], or other MWNT nanocomposites [48].

Equation (5) is fit to the collected data using *MatLab*'s non-linear least-squares function, and the corresponding parameters are reported as a function of the number of bilayers in Table 2. As this table indicates, the thermal properties of our films are linked to thin film thickness. Although R_m is several orders of magnitude higher than R_t, the metallic resistance only contributes 3.3% of the total resistance at room temperature, but the effect is high enough at higher temperatures to account for the positive slope of the resistance response. As a reference for comparison, the fit parameters obtained by Kaiser *et al.* [41] are included in Table 2 as well. It should be noted that the only significant deviation from the SWNT thermal sensitivity is the value of the T_c term, which is two orders of magnitude smaller than that of the $(MWNT\text{-}PSS/PVA)_n$ films. As stated before, this difference is thought to be due to the extra tunneling required due to the presence of PSS and PVA.

The ramifications of these temperature effects on strain sensitivities is not fully known for these particular $(MWNT\text{-}PSS/PVA)_n$ thin films. However, Cao *et al.* [21] has reported that MWNT buckypapers' strain sensitivity increases with temperature. It is hypothesized that this effect will extend to the strain sensitivities of the $(MWNT\text{-}PSS/PVA)_n$ films; however this will be investigated in the future.

Table 2. Fitted parameters of DC resistance response to monotonically increasing temperature.

Number of Bi-Layers	R_m [kΩ]	R_t [kΩ]	T_m [10^3 K]	T_c [10^3 K]	T_s [K]
50	610 ± 177	0.310 ± 0.085	1.98 ± 0.26	1.30 ± 0.24	114 ± 19
75	83.9 ± 32.5	0.147 ± 0.047	1.28 ± 0.15	1.13 ± 0.09	57.7 ± 8.5
100	68.0 ± 20.7	0.194 ± 0.055	1.19 ± 0.10	1.11 ± 0.08	48.9 ± 4.8
150	21.5 ± 5.0	0.108 ± 0.022	0.99 ± 0.09	1.01 ± 0.07	45.2 ± 7.8
SWNT-Rope [41]	-	-	~2.00	0.065	42

With regards to the thermal-resistive behavior, it is not fully understood why the $(MWNT\text{-}PSS/PVA)_n$ films have responded to temperature in a manner like that of SWNTs. It is hypothesized that this is due to the fact that the MWNTs used in this study are less than 8 nm in diameter. This translates to MWNTs having very few walls. Although the difference in electronic properties has been investigated between SWNTs and MWNTs, it is not clear how these properties affect the thermal-electronic coupling, and more work is necessary in the future.

3.5 Humidity Response

The responses of the $(MWNT\text{-}PSS/PVA)_n$ thin films to monotonically increasing humidity levels are highly non-linear, as indicated by the DC resistance responses shown in figure 14. Figure 14 plots a representative response from each of the thin film thickness sample sets. Plotted with a *y*-axis logarithmic scale, it is easy to see that thin film electrical responses to humidity are bi-functional in nature, possessing two regions of different exponential sensitivity. Using a sigmoidal function to relate two exponential functions, the data has been fit to the following equation:

$$\frac{\Delta R}{R_0}(\%RH) = \frac{1}{2}\left(1 - erf(\%RH - H_{Tr})\right)\cdot H_1 e^{f_1(\%RH)} + \frac{1}{2}\left(erf(\%RH - H_{Tr}) + 1\right)\cdot H_2 e^{f_2(\%RH)} \quad (6)$$

In equation (6), *erf( )* is the error function, which is in the sigmoidal class of functions that returns a sharp transition between -1 and 1, thereby allowing for a transition to be made between the two exponential functions. The average fits for each sample set are presented in Table 3. Although swelling of the PSS

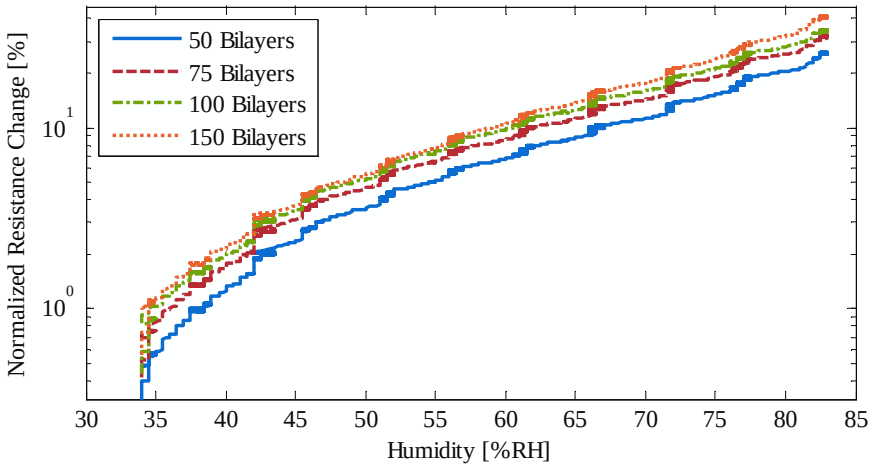

Figure 14. R_{DC} response to increasing humidity levels for 4 representative thin films.

Table 3. Fitted parameters of DC resistance response to monotonically increasing humidity.

Number of Bilayers	H_1	f_1 [%RH]$^{-1}$	H_2	f_2 [%RH]$^{-1}$	H_{Tr} [%RH]
50	$1.01 \pm 0.31 \times 10^{-4}$	0.130 ± 0.002	$3.13 \pm 0.68 \times 10^{-3}$	$5.56 \pm 0.08 \times 10^{-2}$	47.1 ± 0.24
75	$1.08 \pm 0.05 \times 10^{-4}$	0.128 ± 0.001	$3.39 \pm 0.15 \times 10^{-3}$	$5.51 \pm 0.06 \times 10^{-2}$	47.6 ± 0.04
100	$1.07 \pm 0.19 \times 10^{-4}$	0.132 ± 0.005	$3.46 \pm 0.33 \times 10^{-3}$	$5.62 \pm 0.12 \times 10^{-2}$	46.8 ± 0.88
150	$1.87 \pm 0.45 \times 10^{-4}$	0.118 ± 0.022	$2.37 \pm 0.28 \times 10^{-3}$	$6.13 \pm 0.19 \times 10^{-2}$	46.1 ± 0.73

may contribute to this response [49], the full understanding of the underlying mechanisms has yet to be done. However, one can possibly draw a few conclusions from the fit parameters. The first exponential region has a higher sensitivity than the second by about double. This slowing is perhaps due to diffusion of water into the thin film, rather than direct surface absorption when at equilibrium. It should be pointed out that many groups have also found the humidity effect on CNT thin films to be non-linear, and to the best of our knowledge, only limited research has been done to investigate this phenomenon [22, 49, 50].

4. Conclusions

In this work, $(MWNT\text{-}PSS/PVA)_n$ films were manufactured via a LbL process and deposited onto GFRPs. These films were characterized for their sensitivity to applied strain and to environmental changes due to temperature and humidity. Films loaded with monotonically increasing strain to failure demonstrated electrical sensitivity in the time- and frequency domains in a linear-quadratic fashion. It was found that components of the frequency-domain response have higher sensitivity to incurred damage than time-domain DC resistance measurements. Thin film electrical responses to three-cycle dynamic loads to two strain regimes were characterized. It was determined that they continued to function throughout these tests with minimal drift. High-cycle dynamic tests demonstrated the low level drift in the electrical measurements over 1,000 cycles of low-level strain. To determine the sensitivity to temperature changes, the thermal response of the thin films were measured from 20 °C to 100 °C. From these tests, it was found that the $(MWNT\text{-}PSS/PVA)_n$ thin films responded to temperature in a manner more like SWNTs than MWNTs. Finally, their sensitivity to humidity was characterized between 35 %RH and 80 %RH, and the thin film response was found to be bi-exponential in nature. In conclusion, the results produced by this study brought together a better understanding of the electrical responses of LbL MWNT-based films subjected to mechanical, thermal, and hygroscopic variation.

5. Acknowledgements

The authors gratefully acknowledge financial support of this research from the National Science Foundation (grant numbers CAREER CMMI-0642814 and CMMI-1200521) and the College of Engineering, University of California, Davis. Additional support has also been provided by the University of California, Center for Information Technology Research in the Interest of Society (CITRIS) and the Office of Graduate Studies, UC Davis Dissertation Year Fellowship.

References:

[1] Roeseler B, Sarh B, Kismarton M, Quinlivan J, Sutter J and Roberts D 2009 Composite Structures – The First 100 Years Composite Design Tutorial (Stanford University)
[2] Nolet S 2010 Manufacturing of Utility-Scale Wind Turbine Blades Iowa Wind Energy Assoc. 2010 IAWIND Conf. (Ames, IA)
[3] Rosenker M V 2006 Safety Recommendation A-06-27 and -28

[4] Bastianini F, Corradi M, Borri A and Tommaso A 2005 Retrofit and monitoring of an historical building using “Smart” CFRP with embedded fibre optic Brillouin sensors *Construction and Building Materials* **19** 525-535
[5] Park H, Sohn H, Law K and Farrar C 2007 Time reversal active sensing for health monitoring of a composite plate *Journal of Sound and Vibration* **302** 50-66
[6] Mirmiran A and Wei Y 2001 Damage assessment of FRP-encased concrete using ultrasonic pulse velocity *Journal of Engineering Mechanics* **127** 126-135
[7] Rumsey M A and Paquette J A 2008 Structural Health Monitoring of Wind Turbine Blades SPIE Smart Structures / NDE (San Diego, CA, USA)
[8] Qiu Z, Yao X, Yuan J and Soutis C 2006 Experimental research on strain monitoring in composite plates using embedded SMA wires *Smart Materials and Structures* **15** 1047-1053
[9] Tsutsui H, Kawamata A, Sanda T and Takeda N 2004 Detection of damage of composites using embedded optical fibers *Smart Materials and Structures* **13** 1284-1290
[10] Tang H-Y, Winkelmann C, Lestari W and La Saponara V 2011 Composite Structural Health Monitoring Through Use of Embedded PZT Sensors *Journal of Intelligent Material Systems and Structures* **22** 739-755
[11] Iijima S 1991 Helical microtubules of graphitic carbon *Nature* **354** 56-58
[12] Baughman R, Zakhidov A and De Heer W 2002 Carbon nanotubes--the route toward applications *Science* **297** 787
[13] Chou T-W, Gao L, Thostenson E T, Zhang Z and Byun J H 2010 An assessment of the science and technology of carbon nanotube-based fibers and composites *Composites Science and Technology* **70** 1-19
[14] Thostenson E T and Chou T-W 2006 Carbon nanotube networks: sensing of distributed strain and damage for life prediction and self healing *Advanced Materials* **18** 2837-2841
[15] Rein M, Breuer O and Wagner H 2011 Sensors and sensitivity: Carbon nanotube buckypaper films as strain sensing devices *Composites Science and Technology* **71** 373-381
[16] Dharap P, Li Z, Nagarajaiah S and Barrera E 2004 Nanotube film based on single-wall carbon nanotubes for strain sensing *Nanotechnology* **15** 379-382
[17] Kang I, Schulz M J, Kim J H, Shanov V and Shi D 2006 A carbon nanotube strain sensor for structural health monitoring *Smart Materials and Structures* **15** 737
[18] Loh K J, Lynch J P, Shim B S and Kotov N A 2008 Tailoring piezoresistive sensitivity of multilayer carbon nanotube composite strain sensors *Journal of Intelligent Material Systems and Structures* **19** 747-764
[19] Hu N, Karube Y, Arai M, Watanabe T, Yan C, Li Y, Liu Y and Fukunaga H 2010 Investigation on sensitivity of a polymer/carbon nanotube composite strain sensor *Carbon* **48** 680-687
[20] Loyola B R, La Saponara V and Loh K J 2010 In Situ Strain Monitoring of Fiber-Reinforced Polymers using Embedded Piezoresistive Nanocomposites *Journal of Material Science* **45** 6786-6798
[21] Cao C L, Hu C G, Xiong Y F, Han X Y, Xi Y and Miao J 2007 Temperature dependent piezoresistive effect of multi-walled carbon nanotube films *Diamond and Related Materials* **16** 388-392
[22] Yu H, Cao T, Zhou L, Gu E, Yu D and Jiang D 2006 Layer-by-Layer assembly and humidity sensitive behavior of poly(ethyleneimine)/multiwall carbon nanotube composite films *Sensors and Actuators B: Chemical* **119** 512-515
[23] National Instruments 2012 How Is Temperature Affecting Your Strain Measurement Accuracy?
[24] Patrick H, Williams G, Kersey A, Pedrazzani J and Vengsarkar A 1996 Hybrid fiber Bragg grating/long period fiber grating sensor for strain/temperature discrimination *Photonics Technology Letters, IEEE* **8** 1223-1225
[25] Decher G and Schlenoff J B 2003 *Multilayer Thin Films* (Weinheim, Germany:Wiley-VCH)
[26] Schlenoff J and Dubas S 2001 Mechanism of polyelectrolyte multilayer growth: Charge overcompensation and distribution *Macromolecules* **34** 592-598

[27] Chen C-h, LaRue J C, Nelson R D, Kulinsky L and Madou M J 2012 Electrical conductivity of polymer blends of poly(3,4-ethylenedioxythiophene): Poly(styrenesulfonate): N-methyl-2-pyrrolidinone and polyvinyl alcohol *Journal of Applied Polymer Science* **125** 3134-3141
[28] O'Connell M J, Boul P, Ericson L M, Huffman C, Wang Y, Haroz E, Kuper C, Tour J, Ausman K D and Smalley R E 2001 Reversible water-solubilization of single-walled carbon nanotubes by polymer wrapping *Chemical Physics Letters* **342** 265-271
[29] Zhao Y, Loyola B R and Loh K J 2011 Mechanical and Viscoelastic Characterization of Layer-by-Layer Carbon Nanotube-Polyelectrolyte Thin Films *Smart Materials and Structures* **20** 075020
[30] ASTM International 2008 ASTM D3039 / D3039M - 08 Standard Test Method for Tensile Properties of Polymer Matrix Composite Materials
[31] Loh K J, Kim J, Lynch J P, Kam N W S and Kotov N A 2007 Multifunctional layer-by-layer carbon nanotube polyelectrolyte thin films for strain and corrosion sensing *Smart Materials and Structures* **16** 429-438
[32] Bauerle J 1969 Study of solid electrolyte polarization by a complex admittance method *Journal of Physics and Chemistry of Solids* **30** 2657-2670
[33] Kota A K, Cipriano B H, Duesterberg M K, Gershon A L, Powell D, Raghavan S R and Bruck H A 2007 Electrical and rheological percolation in polystyrene/MWCNT nanocomposites *Macromolecules* **40** 7400-7406
[34] McClory C, Pötschke P and McNally T 2011 Influence of Screw Speed on Electrical and Rheological Percolation of Melt-Mixed High-Impact Polystyrene/MWCNT Nanocomposites *Macromolecular Materials and Engineering* **296** 59-69
[35] De S, Lyons P E, Sorel S, Doherty E M, King P J, Blau W J, Nirmalraj P N, Boland J J, Scardaci V and Joimel J 2009 Transparent, flexible, and highly conductive thin films based on polymer−nanotube composites *ACS Nano* **3** 714-720
[36] Ma Y, Cheung W, Wei D, Bogozi A, Chiu P L, Wang L, Pontoriero F, Mendelsohn R and He H 2008 Improved conductivity of carbon nanotube networks by in situ polymerization of a thin skin of conducting polymer *ACS Nano* **2** 1197-1204
[37] Kang I, Schulz M, Kim J, Shanov V and Shi D 2006 A carbon nanotube strain sensor for structural health monitoring *Smart Materials and Structures* **15** 737-748
[38] Thostenson E T and Chou T-W 2008 Real-time in situ sensing of damage evolution in advanced fiber composites using carbon nanotube networks *Nanotechnology* **19** 215713
[39] Shindo Y, Kuronuma Y, Takeda T, Narita F and Fu S Y 2011 Electrical resistance change and crack behavior in carbon nanotube/polymer composites under tensile loading *Composites Part B: Engineering* 39-43
[40] Gao L, Thostenson E T, Zhang Z and Chou T-W 2009 Coupled carbon nanotube network and acoustic emission monitoring for sensing of damage development in composites *Carbon* **47** 1381-1388
[41] Kaiser A, Düsberg G and Roth S 1998 Heterogeneous model for conduction in carbon nanotubes *Physical Review B* **57** 1418–1421
[42] Barnes T M, Blackburn J L, van de Lagemaat J, Coutts T J and Heben M J 2008 Reversibility, Dopant Desorption, and Tunneling in the Temperature-Dependent Conductivity of Type-Separated, Conductive Carbon Nanotube Networks *ACS Nano* **2** 1968-1976
[43] Wei X and Tianhong C 2007 Characterization of layer-by-layer self-assembled carbon nanotube multilayer thin films *Nanotechnology* **18** 145709
[44] Charlier J C and Issi J P 1998 Electronic structure and quantum transport in carbon nanotubes *Applied Physics A: Materials Science & Processing* **67** 79-87
[45] Langer L, Bayot V, Grivei E, Issi J P, Heremans J, Olk C, Stockman L, Van Haesendonck C and Bruynseraede Y 1996 Quantum transport in a multiwalled carbon nanotube *Physical review letters* **76** 479-482
[46] Ding W, Pengcheng S, Changhong L, Wei W and Shoushan F 2008 Highly oriented carbon nanotube papers made of aligned carbon nanotubes *Nanotechnology* **19** 075609

[47] Zhang M, Fang S, Zakhidov A A, Lee S B, Aliev A E, Williams C D, Atkinson K R and Baughman R H 2005 Strong, Transparent, Multifunctional, Carbon Nanotube Sheets *Science* **309** 1215-1219
[48] Fung C K M and Li W J 2004 Ultra-low-power polymer thin film encapsulated carbon nanotube thermal sensors
[49] Shim B S, Chen W, Doty C, Xu C and Kotov N A 2008 Smart electronic yarns and wearable fabrics for human biomonitoring made by carbon nanotube coating with polyelectrolytes *Nano letters* **8** 4151-4157
[50] Tang Q-Y, Chan Y C and Zhang K 2011 Fast response resistive humidity sensitivity of polyimide/multiwall carbon nanotube composite films *Sensors and Actuators B: Chemical* **152** 99-106

Figure 2a (Final Figures/Figure_2a.JPG)

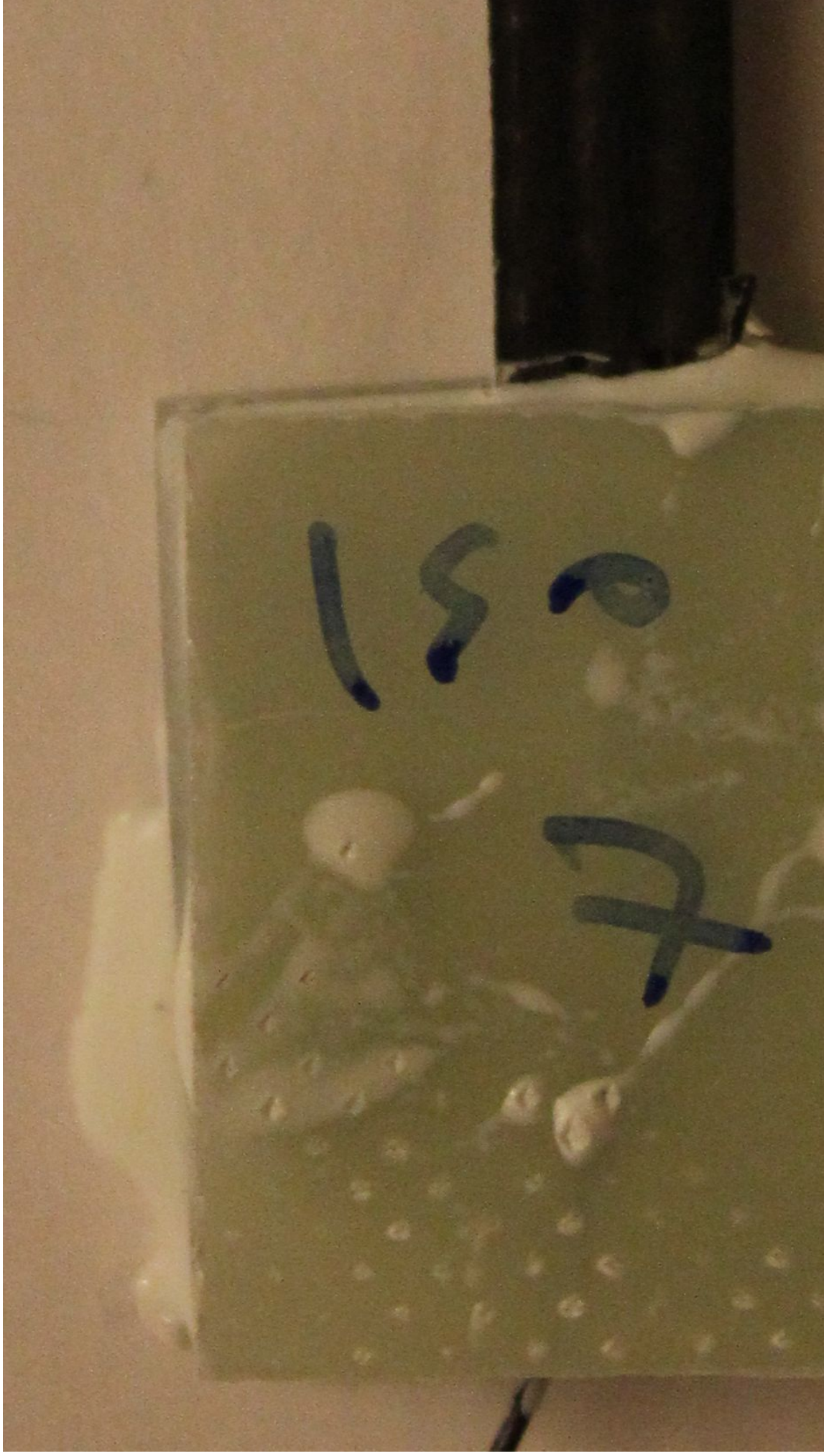

Figure 2b (Final Figures/Figure_2b.jpg)

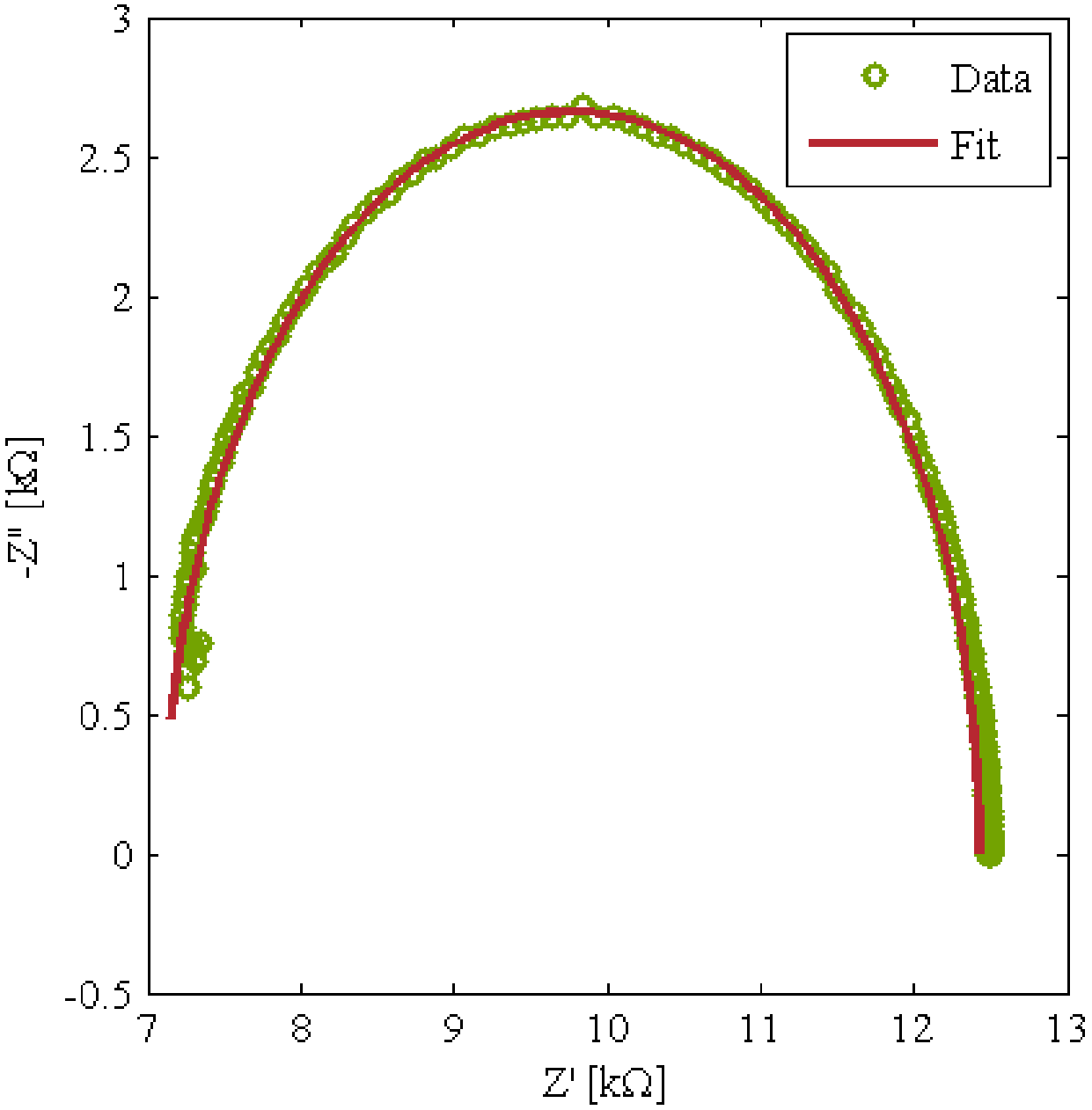

Figure 3 (Final Figures/Figure_3.tif)

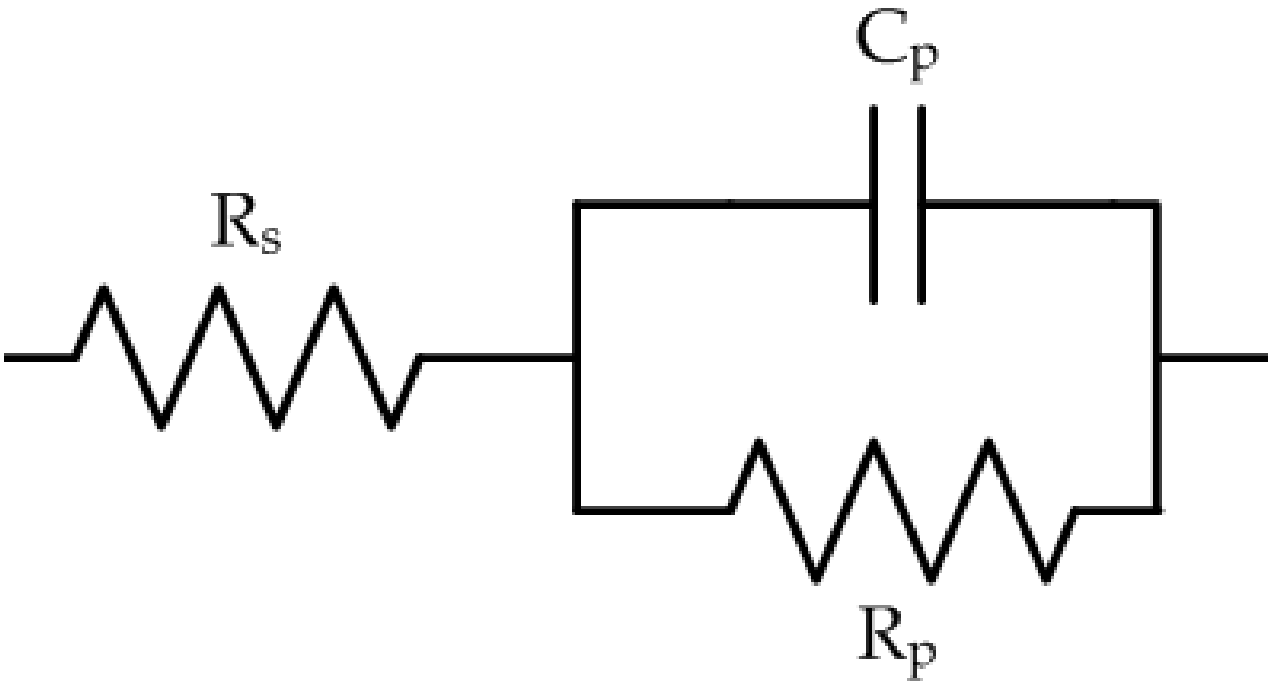

Figure 4 (Final Figures/Figure_4.tif)

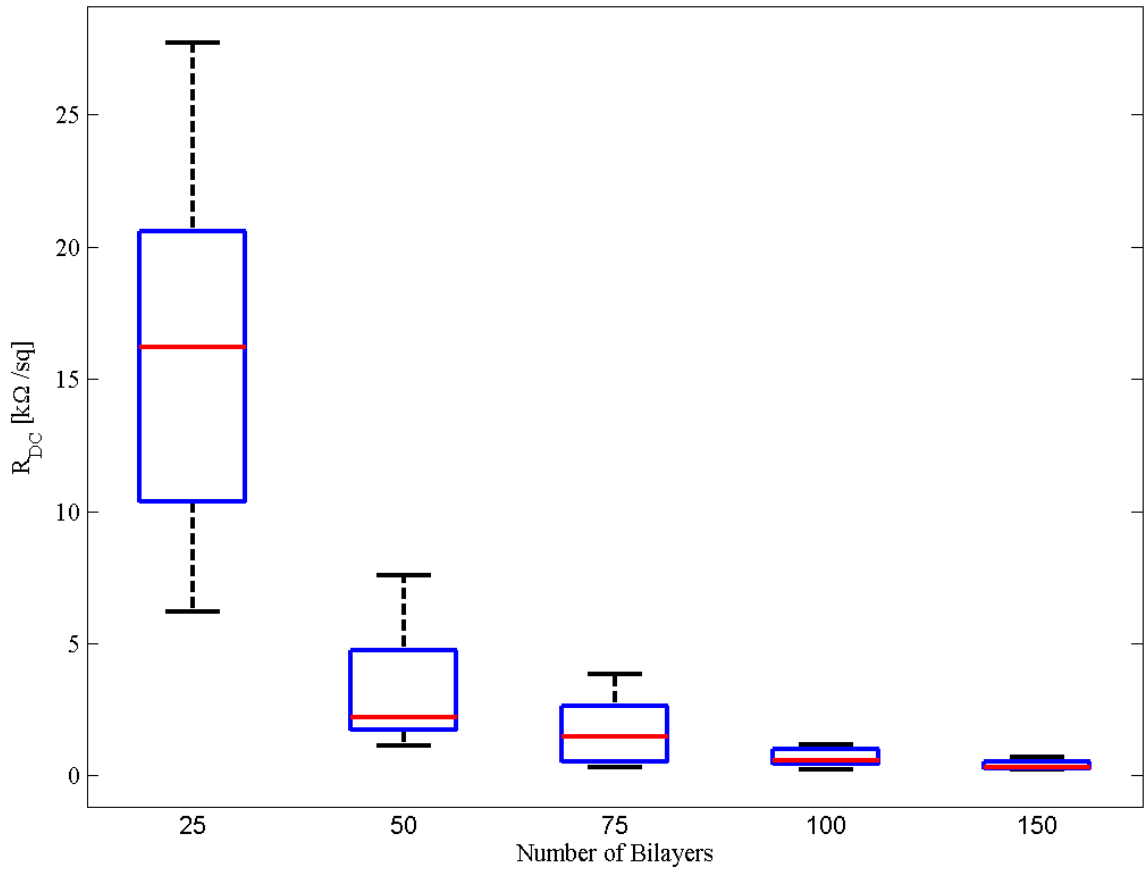

Figure 5a (Final Figures/Figure_5a.tiff)

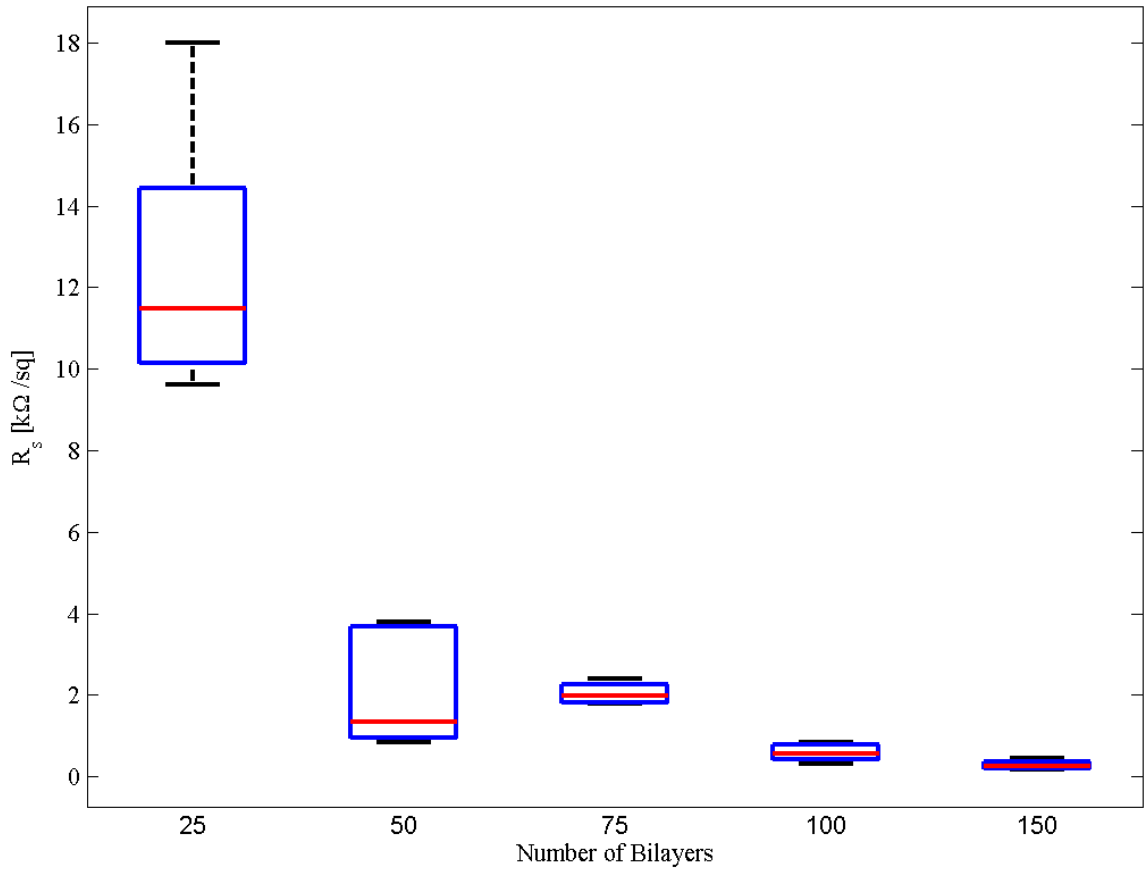

Figure 5b (Final Figures/Figure_5b.tiff)

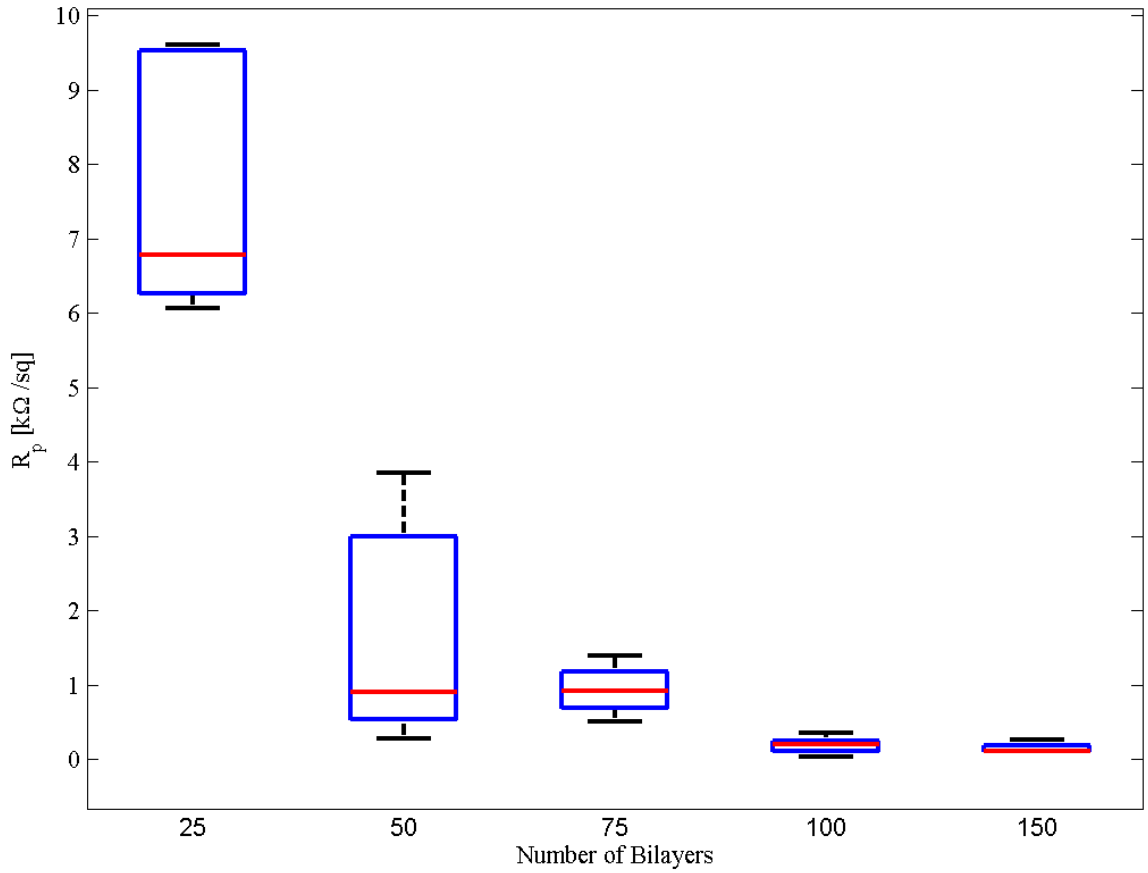

Figure 5c (Final Figures/Figure_5c.tiff)

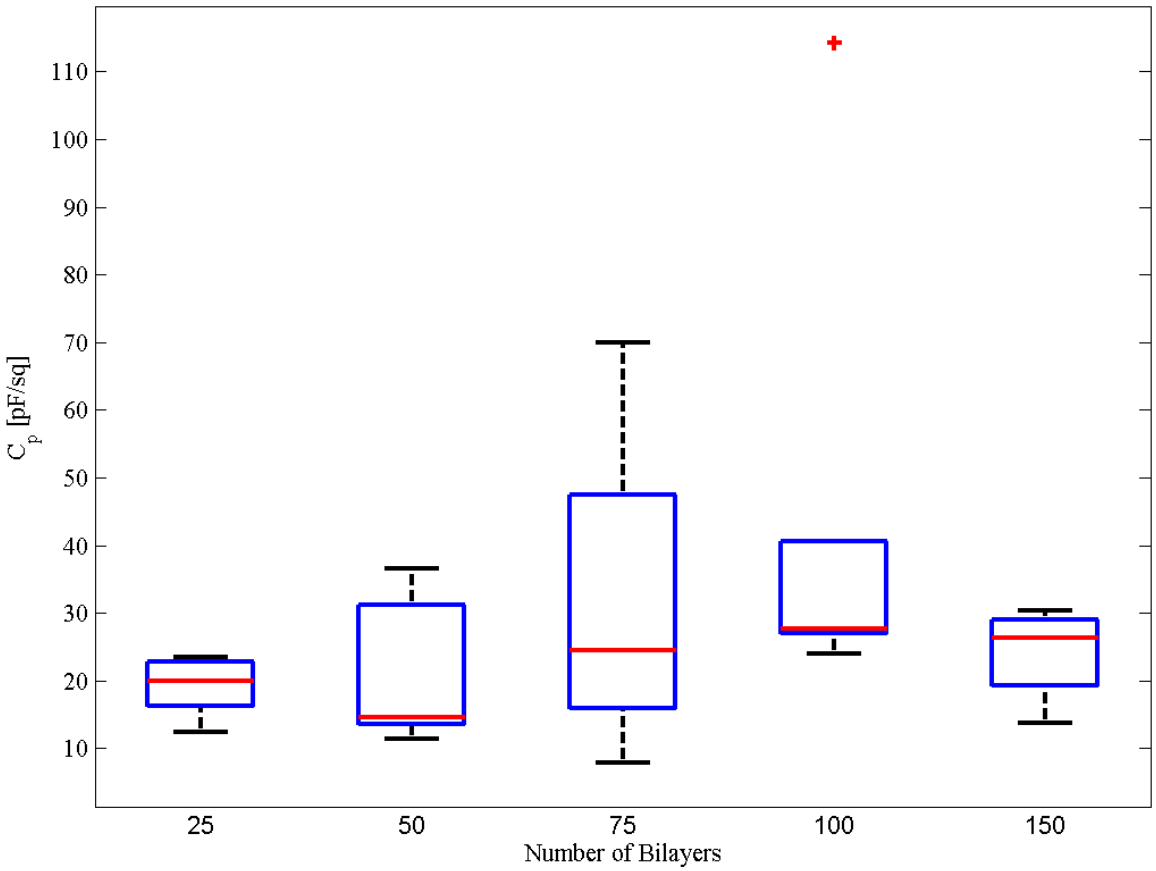

Figure 5d (Final Figures/Figure_5d.tiff)

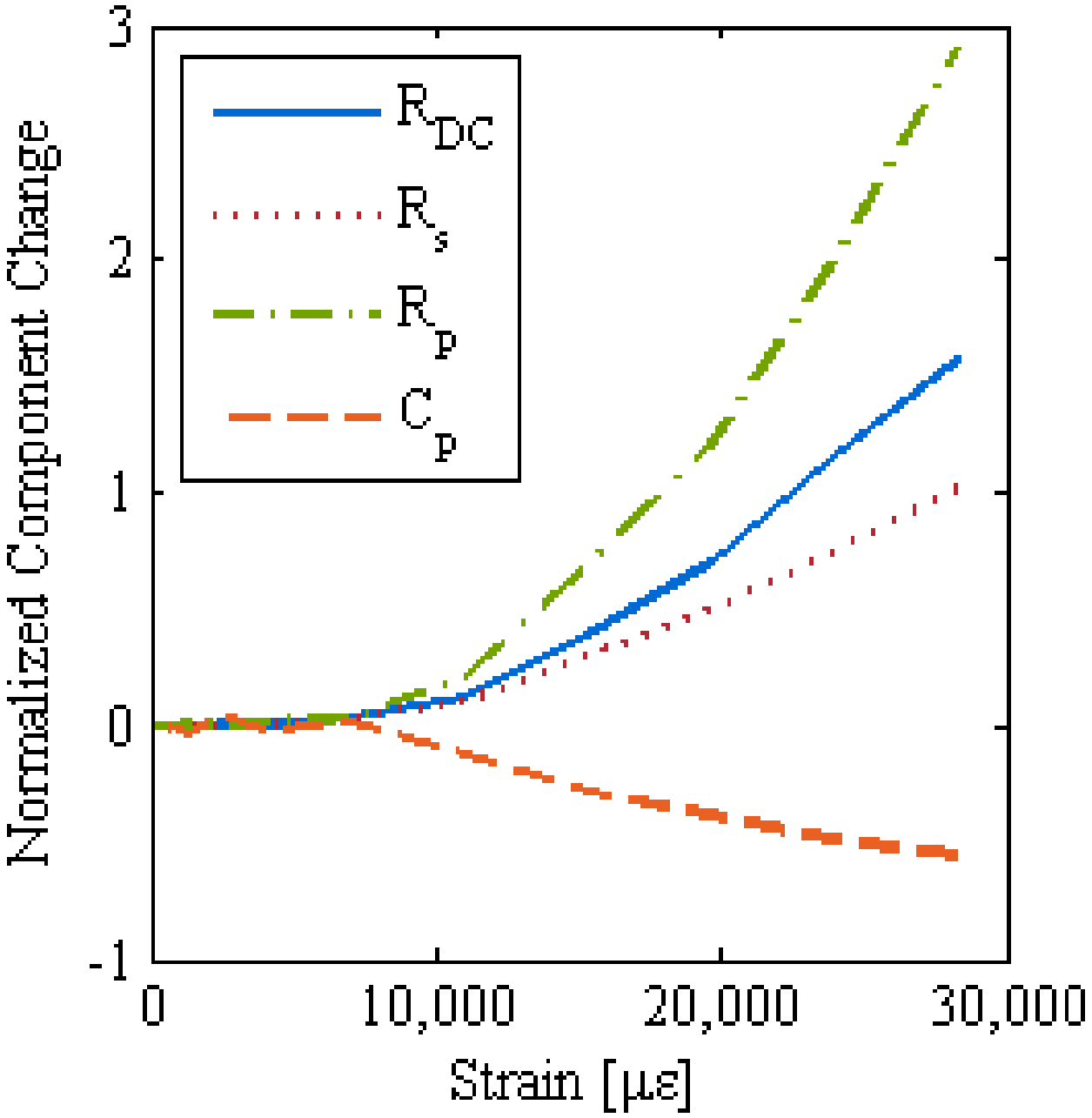

Figure 6 (Final Figures/Figure_6.tif)

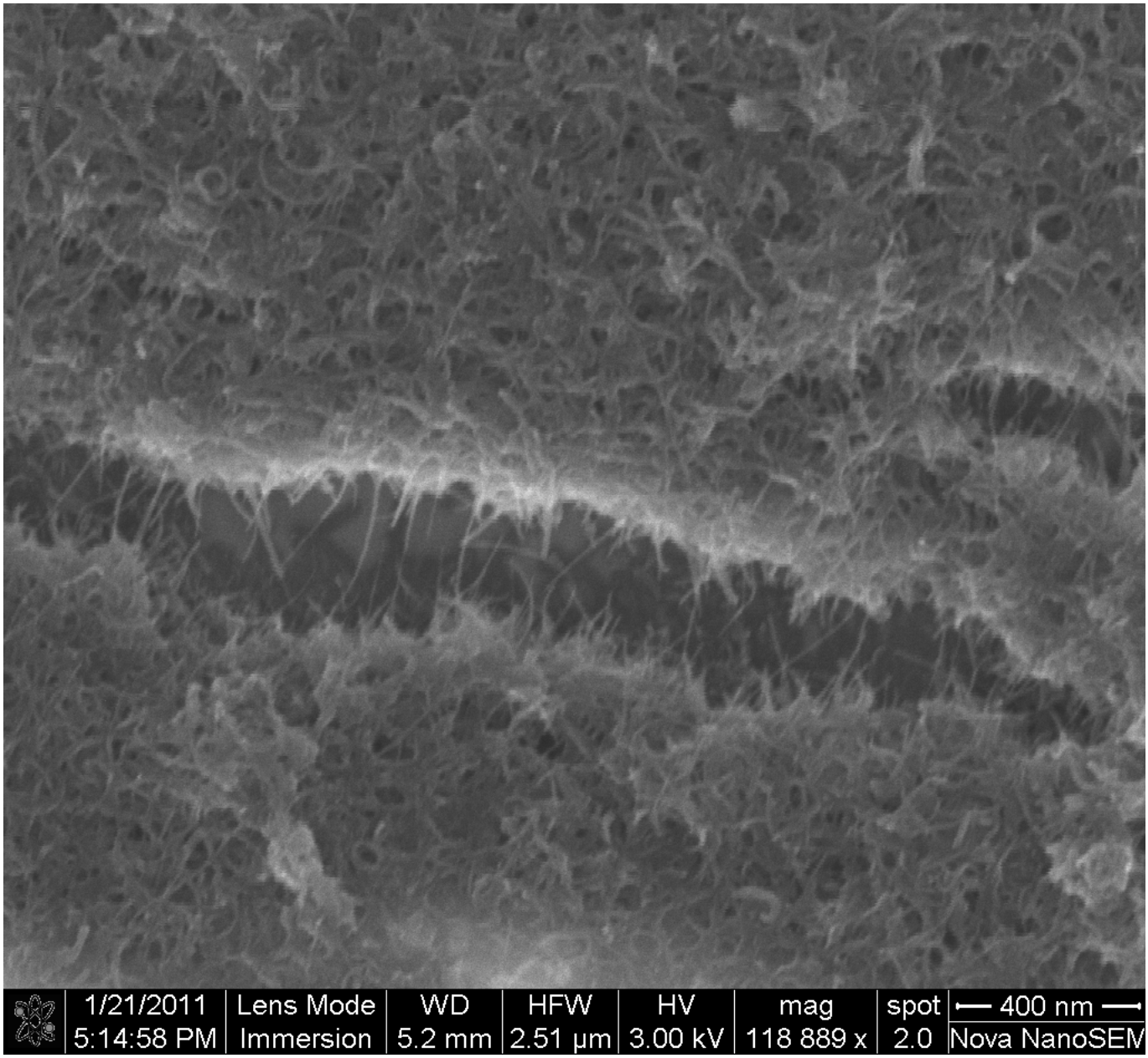

Figure 7 (Final Figures/Figure_7.tif)

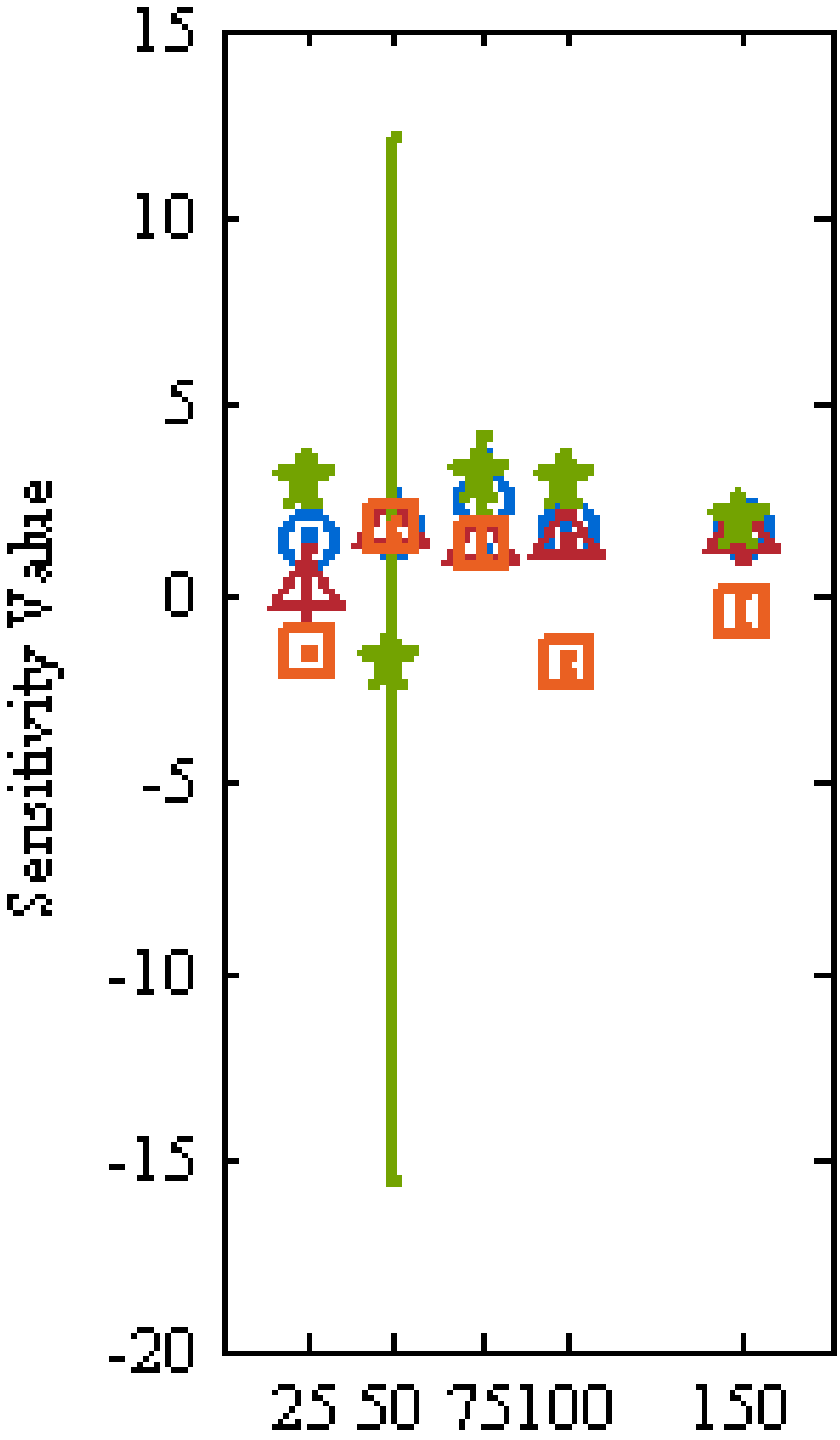

Figure 8a (Final Figures/Figure_8a.tif)

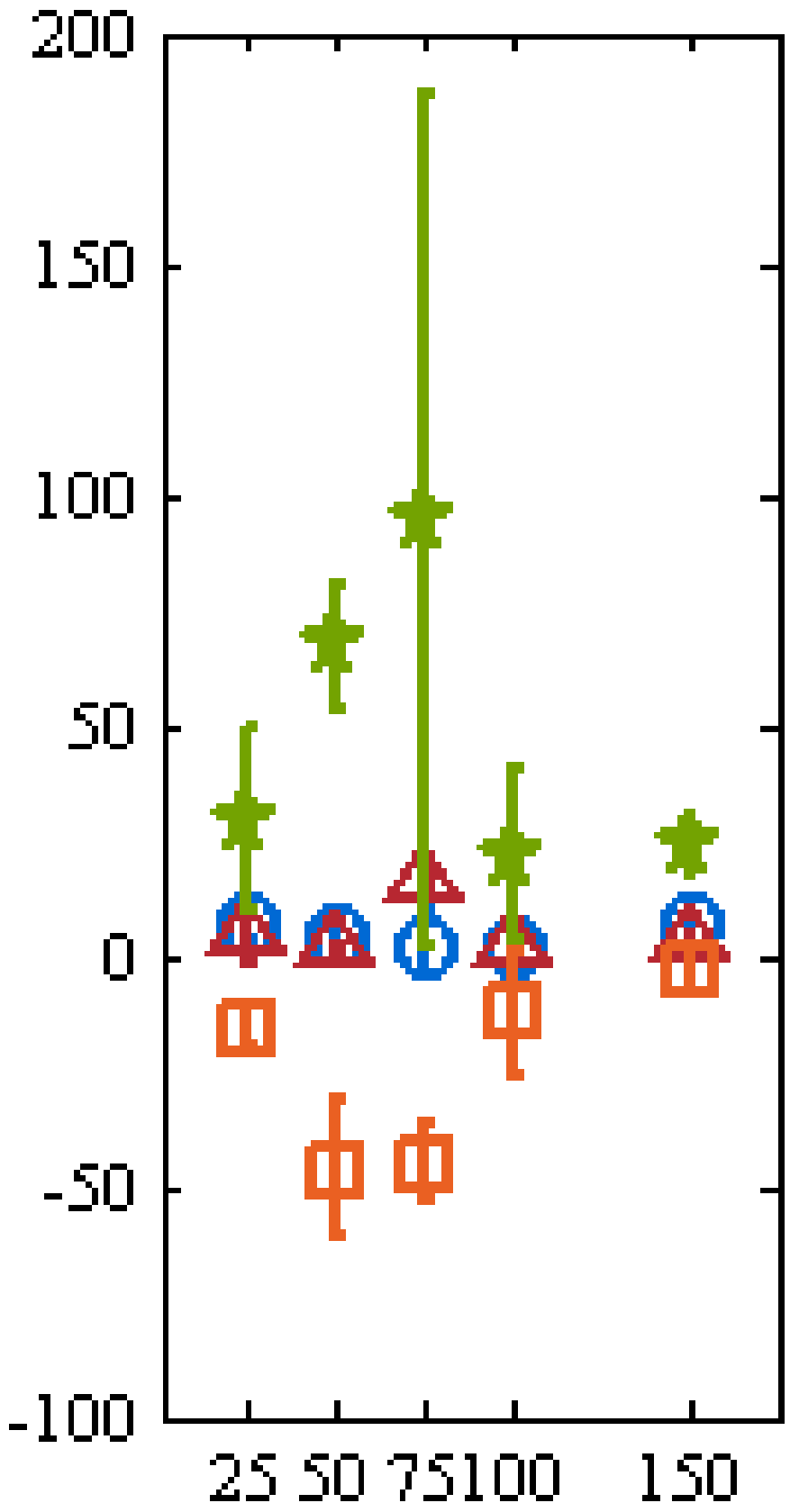

Figure 8b (Final Figures/Figure_8b.tif)

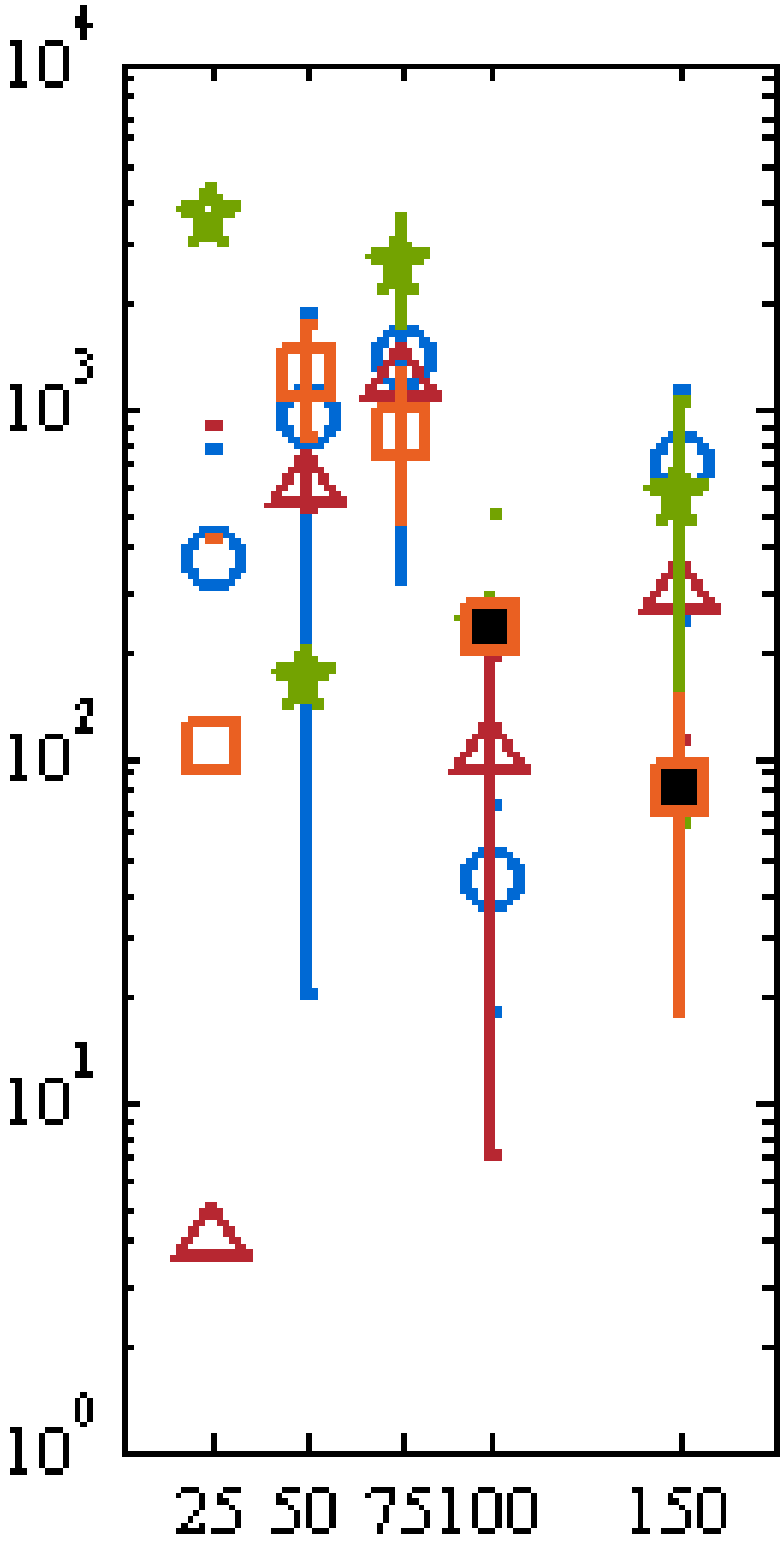

Figure 8c (Final Figures/Figure_8c.tif)

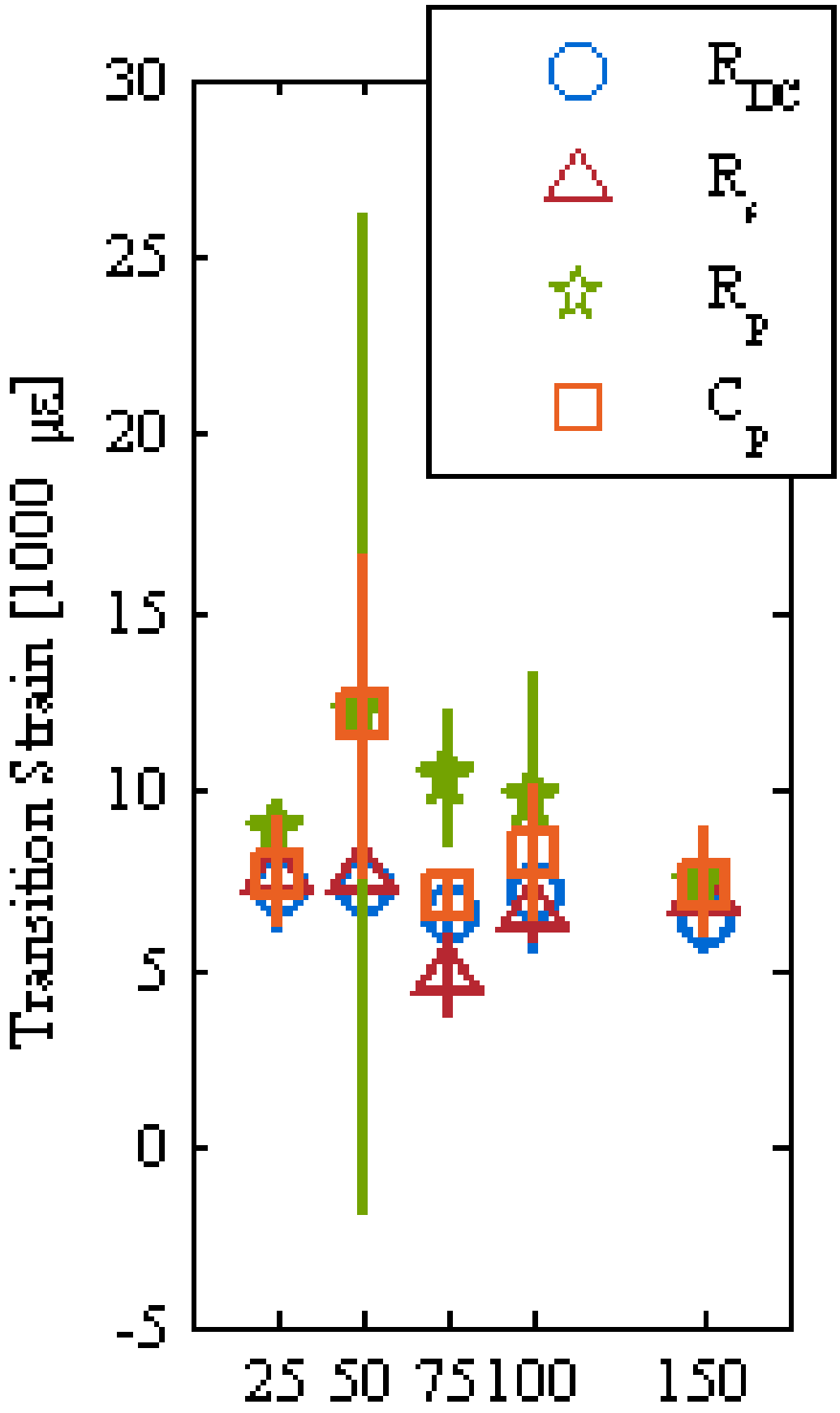

Figure 8d (Final Figures/Figure_8d.tif)

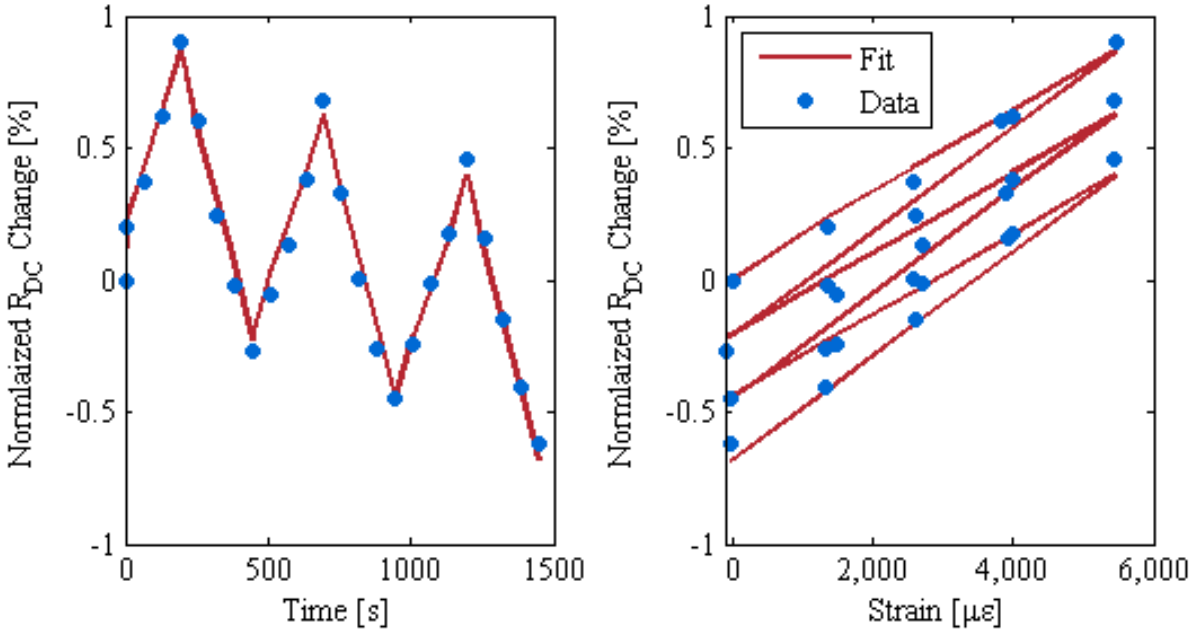

Figure 9 (Final Figures/Figure_9.tif)

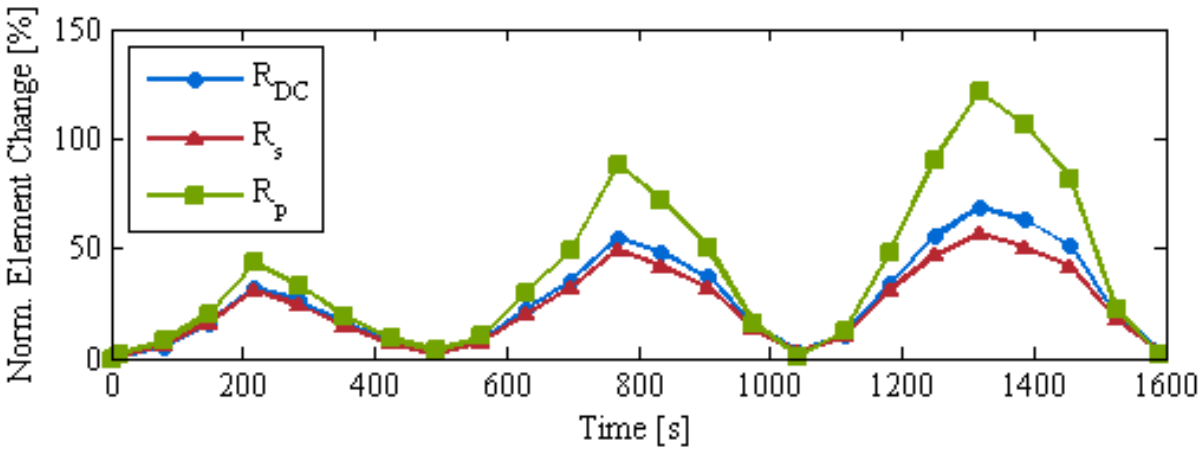

Figure 10 (Final Figures/Figure 10.tif)

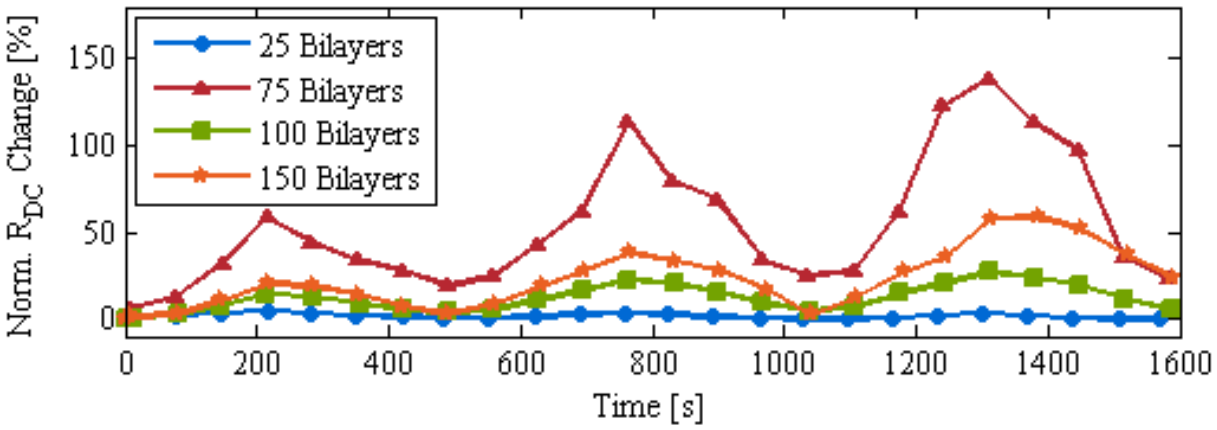

Figure 11 (Final Figures/Figure_11.tif)

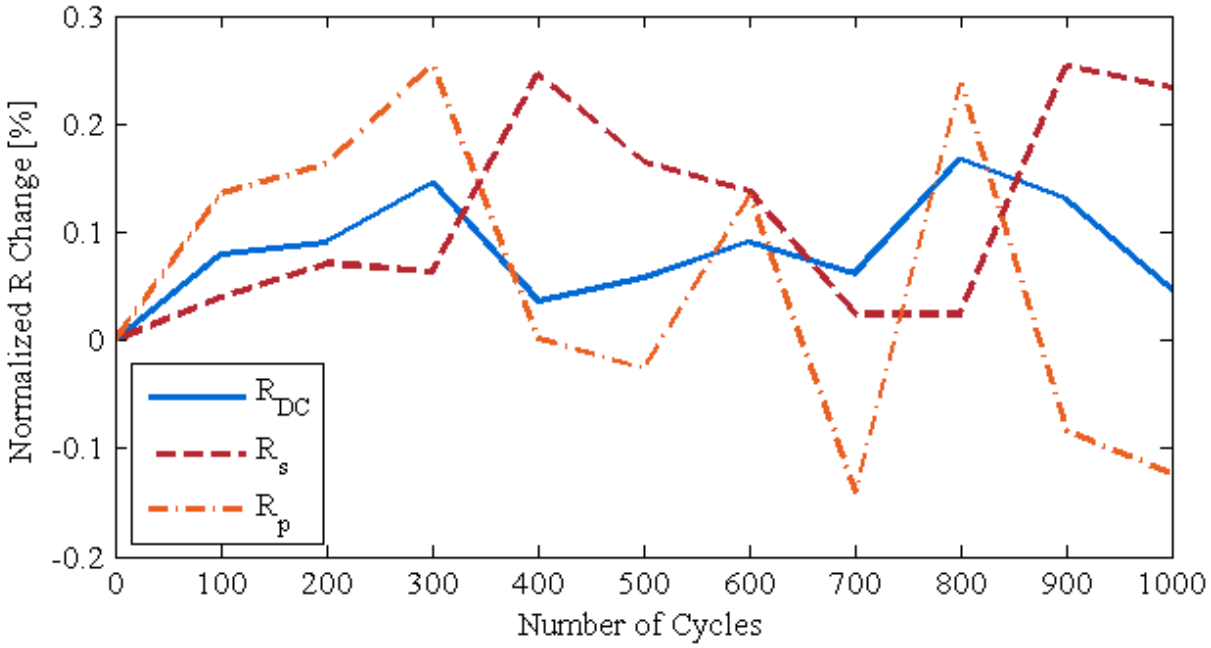

Figure 12 (Final Figures/Figure_12.tif)

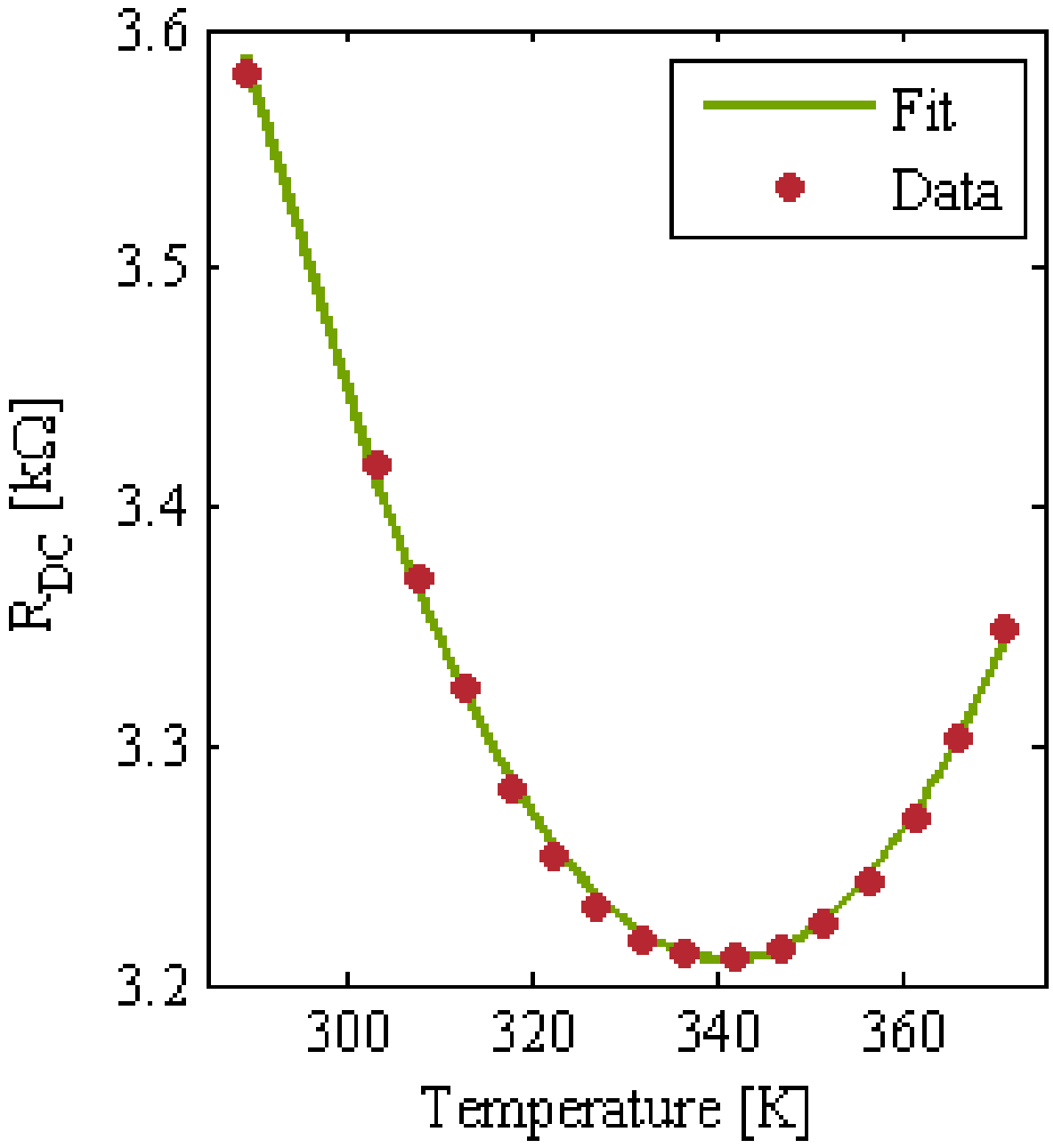

Figure 13 (Final Figures/Figure_13.tif)

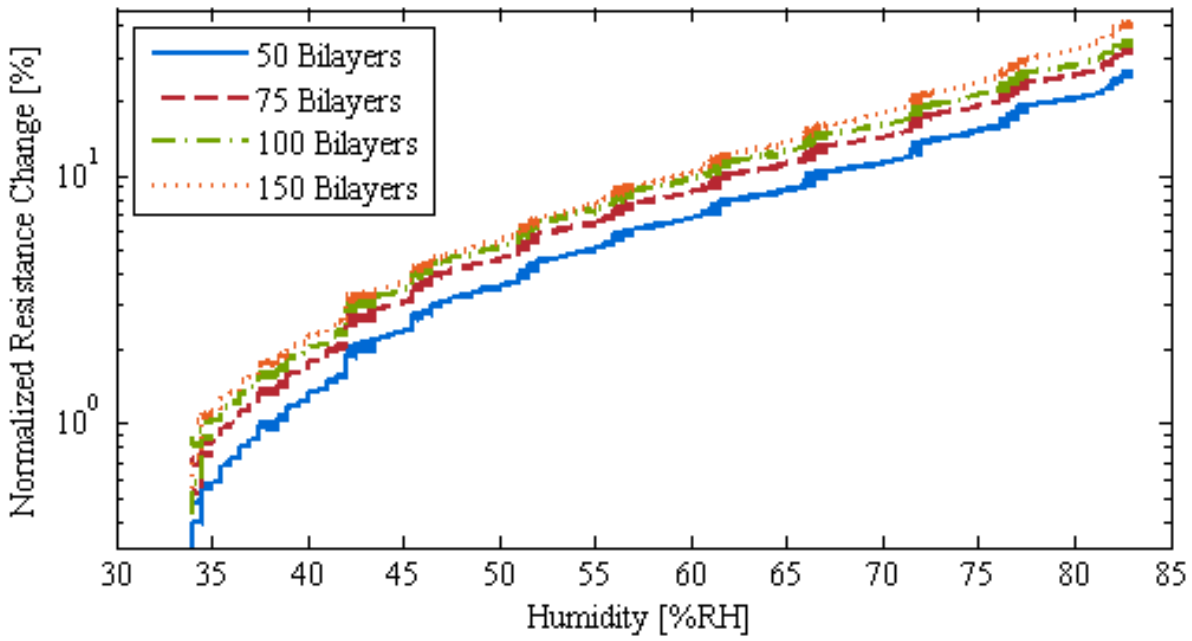

Figure 14 (Final Figures/Figure_14.tif)